IMT School for Advanced Studies, Lucca
Lucca, Italy

DELAMINATION OF THIN LAYERS PROMOTED BY LOCAL BUCKLING

PhD Program in Institutions, Markets and Technologies

Curriculum in Computer Science and Systems Engineering

XXXII Cycle

By

Nicola Dardano

2022

The dissertation of Nicola Dardano is approved.

PhD Program Coordinator: Prof. Rocco De Nicola, IMT School for Advanced Studies Lucca

Advisor: Prof. Marco Paggi, IMT School for Advanced Studies Lucca

Co-Advisor: Prof. Stefano Bennati, University of Pisa

Co-Advisor: Prof. Paolo Sebastiano Valvo, University of Pisa

The dissertation of Nicola Dardano has been reviewed by:

Prof. Elena Benvenuti, University of Ferrara

Prof. Nicola Luigi Rizzi, University Roma Tre

IMT School for Advanced Studies Lucca
2022

Contents

List of Figures

List of Tables

Acknowledgements

I would like to thank my advisors: Prof. Marco Paggi, Prof. Stefano Bennati and, in particular, Prof. Paolo Sebastiano Valvo for their rigorous guidance and their attention to this work.

I would like to thank the external referees: Prof. Elena Benvenuti and Prof. Nicola Rizzi for the time and the attention devoted to the revision of the thesis. I tried to take advantage from their suggestions to improve the presentation of the thesis.

I am very grateful to my friends and colleagues form IMT, MUSAM and MAMas Research group.

I am very grateful to Prof. Daniele Fanteria and the company Microtex S.r.l. for the specimens providing.

Finally, I want to thank my family and my friends.

Abstract

This dissertation investigates the combined phenomena of buckling and fracture, which occur in thin superficial layers subjected to compressive forces. As a representative case, the four-point bending test on laminated specimens with mid-span, through-the-width delaminations, is taken into consideration: a mechanical model of the test was developed and experimental tests on carbon fiber laminates were conducted. The thesis is subdivided into six Chapters. Chapter 1 presents a general introduction to the investigated problem. Chapter 2 illustrates the state of the art on delamination in composite materials with focus on buckling-driven delamination and four-point bending tests. Chapter 3 illustrates the experimental Mode II fracture toughness characterization of the carbon fiber laminates investigated in the thesis. In Chapter 4, the experimental campaign with four-point bending tests is illustrated. Chapter 5 presents the analytical model to simulate and interpret the four-point bending tests. Chapter 6 shows a comparison between the analytical prediction and the experimental evidence. In Chapter 7, results are summarized and future developments are outlined.

Chapter 1

Introduction

The detachment of a thin superficial layer from an underlying substrate due to the combined action of local buckling and fracture propagation, is a damage mode common to many technological applications and natural objects from the nano scale of thin superficial layers (Figure 1) to the macro scale of civil engineering constructions (Figure 2).

Among layered structures and material, fiber reinforced composite laminates – made up of several fiber reinforced laminae stacked on top of each others – play a central role in contemporary engineering. Thanks to their high strength and stiffness to weight ratios, composites are used for high-performance structural applications in both civil and industrial engineering [41]. Conversely, composites are prone to a number of damage phenomena [81]. Delamination is one of the most critical issues for the integrity and the mechanical performance of fiber-reinforced composite laminates. Delamination cracks in composite laminates may originate from manufacturing defects, low-energy impacts, and many other causes [82, 72].

Once present, a delamination crack can propagate because of high interlaminar stresses. Thesecan be produced by different loading conditions. A particularly dangerous case is when a superficial layer of a composite structural element is loaded under compression (due to applied

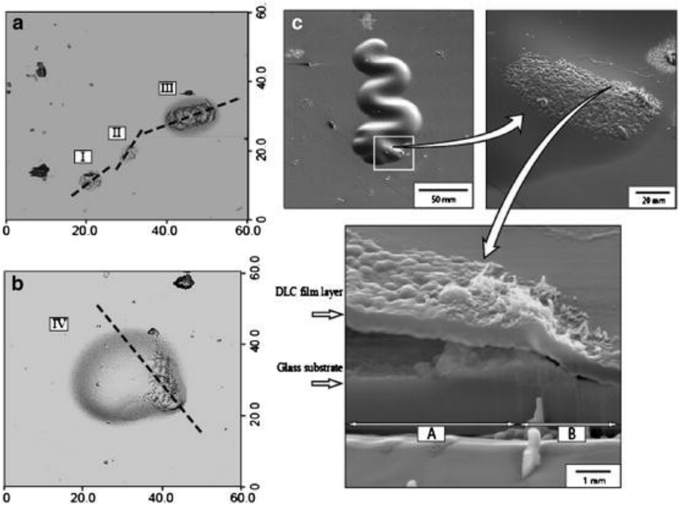

Figure 1: Buckling delamination of compressed thin films [56]

loads, thermal and/or residual stresses). The regions where bonding is weak or missing may undergo local buckling. As a consequence, high stresses arise at the crack front, thus promoting the further expansion of the debonded region [15].

To investigate experimentally buckling driven delamination in composites, many authors have suggested to carry out four-point bending tests on laminated specimens with mid-span, through-the-width delamination cracks [44, 48, 49, 50, 38, 39].

In the present thesis, a mechanical model to describe the four - point bending tests on delaminated specimens was developed. The work started by extending an approach already adopted to analyze delamination buckling in a different problem [8, 9]. Initially, we modeled the specimen as an assemblage of sub-laminates partially connected by an elastic interface [12]. Nevertheless, the elastic - interface model exhibits problems both from analytical and numerical points of view. Despite the elastic interface gave us the possibility to evaluate directly the interlaminar stresses, we decided to avoid the use of the elastic interface. Them, to compute the energy release rate and the modal contributions, we used the methodol-

Figure 2: Buckling delamination of a sidewalk steel grid

ogy proposed in [85]. The energy release rate and mode mixity were evaluated to predict the load corresponding to the onset of delamination growth by adopting the mixed - mode fracture criterion proposed by Hutchinson and Suo [40].

In our mechanical model (Figure 3) thanks to the symmetry the analysis is limited to the left-hand half of the specimen. This is subdivided into two zones: a first zone, between the support and the crack tip, where the specimen is modelled as a single laminate; a second zone, between the crack tip and the symmetry axis, where the two previous sub-laminates are not connected. All sub-laminates are considered as extensible and flexible beams undergoing small elastic deformations, except for the compressed sub-laminate in the second zone, which may undergo large displacements. The mechanical problem is described by a set of differential equations with suitable boundary conditions, which are solved analytically. The buckling load is then determined numerically.

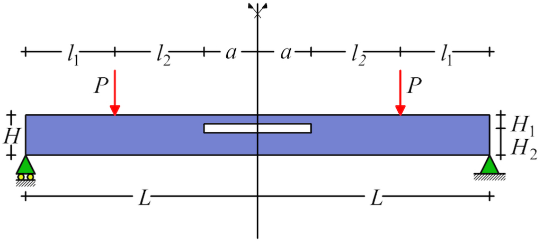

Figure 3: Mechanical model

An extensive experimental campaign to validate the proposed mechanical model was conducted. A set of specimens was provided by Miroctex Composites S.r.l., Prato. The Manufacturer provided us the longitudinal Youngs modulus (E_{11}), the tangential elasticity modulus (G_{31}) and fracture toughness in pure mode I (G_{IC}). But, it was necessary to characterize fracture toughness also in pure mode II (G_{IIc}). In fact, bending induces a mixed mode I/II stress state at the crack tip, which produces its further crack propagation. For this reason, first of all, end-notched flexural (ENF) tests were carried out on a first series of specimens, as specified by ASTM D7905 /D7905M-14 standard.
Subsequently, a second set of specimens were subjected to four-point (static) bending tests by using the universal testing Machine Zwick/Roell and the Digital Image Correlation (DIC) facilities. This type of test is standardized, but only for monolithic specimens from the ASTM D7264 /D7264M-15. However, we referred to this rule that is also applicable in the case of delaminated samples. It is worth noticing that the delaminated area, which is loaded in compression, at a certain point reaches a critical value and snaps upwards as predicted by the proposed mechanical model. During our experiments, we measured the applied load and the corresponding displacements, as well as the length of the crack and the deformation of the delaminated area by using a DIC technique (Figure 4).

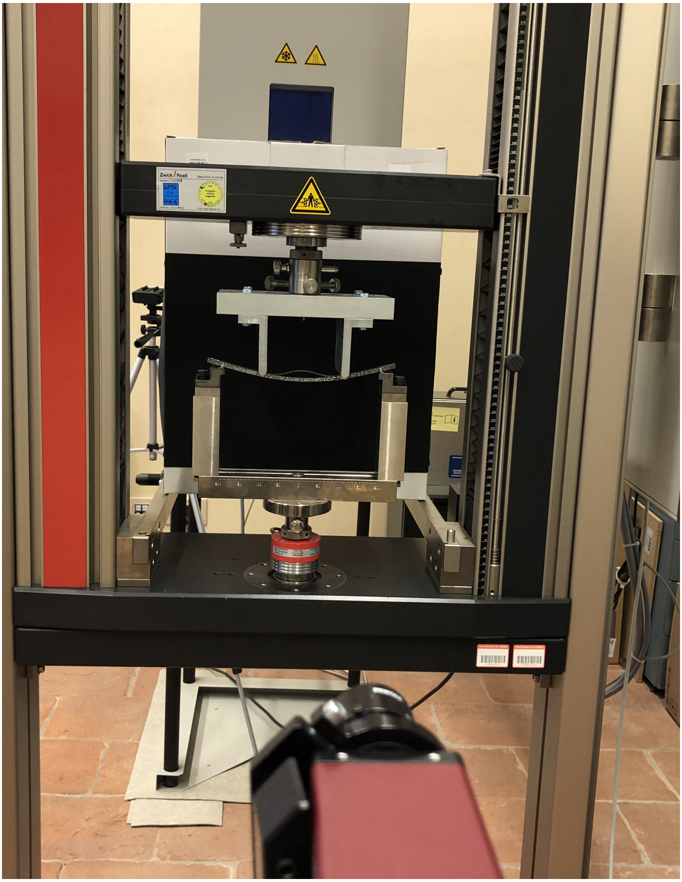

Figure 4: Experimental set up for four-point bending tests

Chapter 2

Literature review

2.1 Introduction to composite materials

Advanced composite materials are widely used in both civil and industrial engineering: e.g. for structural strengthening, aircrafts, wind turbine blades, automotive components and many other applications. This large diffusion originates from the possibilities to build a material with a specific mechanical proprieties. In fact, two or more materials are combined on a macroscopic scale to make a new material. Composite materials differ from homogeneous ones because the components can be identified by the naked eye. If the design of a composite material is optimized, it exibits better qualities than its componets [41]. According to Jones [41], laminates can be divided as follows:

- Fibrous composite materials;
- Laminated (layered) composite materials (Figure 5);
- Particulate composite materials;
- Combination of the previous three.

Fiber-reinforced materials are made by unidirectional or woven fibers in a resin matrix (Figure 6).

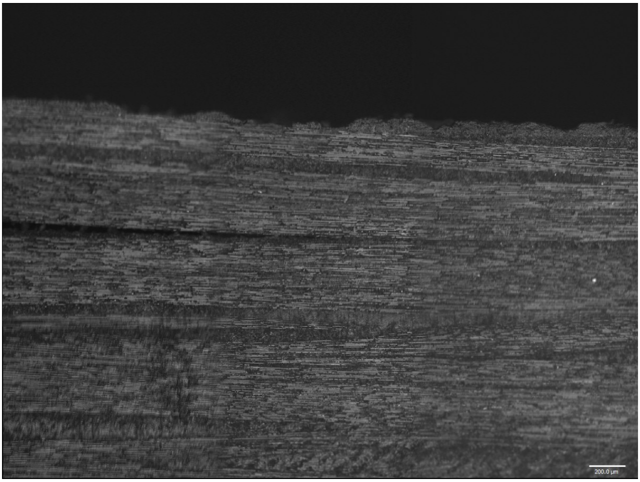

Figure 5: Layered composite material

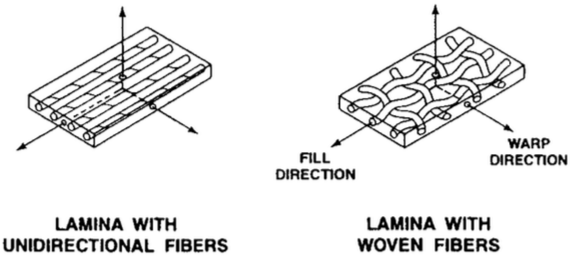

Figure 6: Two principal types of laminae [41]

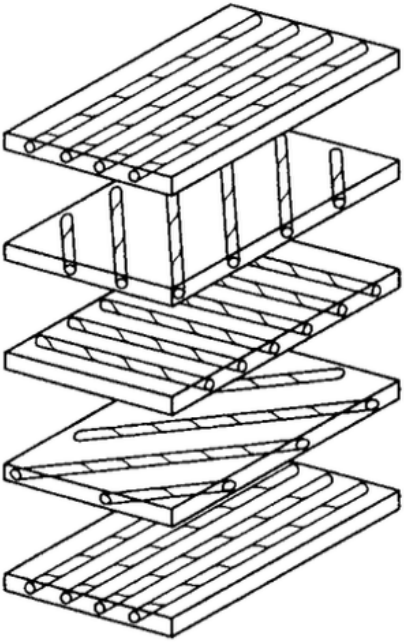

Figure 7: Unbonded view of laminate costruction [41]

The fibers are the main load-bearing of composites: they are strong and stiff. The matrix is a support that protects the fibers and distributes the stresses among fibers. The fibers can be made of glass, carbon, boron, or Kevlar. The matrix is usually a polymeric resin. Laminates are made by a bonded stack of laminae with different orientations (Figure 7). Composite materials have high structural performance, but they can fail due to several damage phenomena. Nowadays, understanding failure in composite materials is an important challenge to avoid damage propagation and save the material integrity.

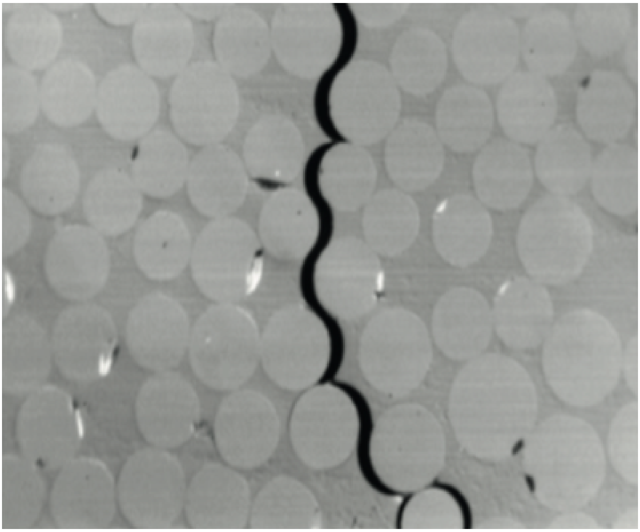

Figure 8: Intralaminar crack initiation from fiber/matrix interface failure. [54]

2.2 Damage in composite materials

2.2.1 Introduction

Due to the heterogeneity of components, composites can be affected by different kinds of damage. In particular, cracks may propagate at different locations: interfacial debonding can arise when the interface between matrix and fibers is weak (Figure 8); matrix microcracking can originate from debonding of fibres and matrix or manufacturing defects, such as inclusions; interfacial sliding can occur between components due to a relative displacement; delamination is a crack that propagate between two different plies in a laminated structure. Delamination can play a relevant role in composite materials failure because, it causes a general weakening of the mechanical properties that govern the composite strength (Figure 9); fiber breakage and fiber microbuckling [81].

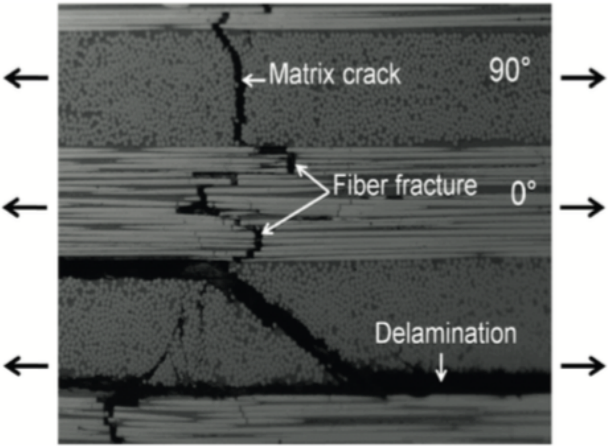

Figure 9: Example of damage modes inlaminates. [54]

2.2.2 Delamination: modelling approaches

Intensive research has been conducted on the delamination of composite laminates during the last decades. On the one hand, theoretical studies have produced both analytical models and numerical methods to predict the onset and growth of delamination cracks [82, 72, 80, 1]. On the other hand, experimental techniques have been developed to assess the interlaminar fracture toughness [18, 22]. In addition, manufacturing techniques have been worked out to improve the delamination resistance of composite laminates [33, 88, 55].

The analysis of delamination is generally carried out in the context of fracture mechanics. By analogy with metals, the earliest studies were based on linear elastic fracture mechanics (LEFM). Thus, the stress - intensity factors, K_I, K_{II}, and K_{III}, or the energy release rate, G, were used as parameters to predict the propagation of delamination cracks [35]. However, in contrast to cracks in isotropic materials, delamination cracks use to propagate according to a mix of the three basic fracture modes (I or opening, II or sliding, and III or tearing), each corresponding to a different delamination toughness, G_{IC}, G_{IIC}, and G_{IIIC}. Con-

sequently, to predict crack growth, the energy release rate has to be suitably decomposed into the sum of three modal contributions, G_I, G_{II}, and G_{III} [40].
To complicate the problem, a number of local damage phenomena such as large-scale fibre - bridging, breakage and buckling of fibres, micro - cracking and plasticisation of the matrix, friction, etc. can take place in the neighbourhood of a delamination crack tip [89]. The size of this damage zone is usually large in comparison with crack length, which contradicts a basic assumption of LEFM [6]. Methods based on non-linear fracture mechanics have been developed [52]. In particular, the cohesive zone model (CZM) originally proposed by Dugdale [34] to investigate plastic fracture and Barenblatt [7] to account for finite strength of brittle materials has been applied to the analysis of delamination in composite laminates. For some cohesive law parameters, a relatively large fracture process zone can develop in the neighbourhood of the crack tip. Here, the fracture surfaces exchange normal and shear stresses, σ and τ, respectively, which depend on the corresponding normal and tangential displacements, Δw and Δu. Several traction-separation relationships, or cohesive laws, have been proposed in the literature. From a mathematical point of view, a first, fundamental distinction is between cohesive laws that can be derived from a potential function, Φ, and those that cannot. The existence of a potential function ensures that the combined work of σ and τ (equivalent to the fracture energy) depends only on the final values of Δw and Δu and not on the load history. Another distinction is between uncoupled cohesive laws, for which is a function of only Δw and τ is a function of only Δu, and coupled cohesive laws, for which σ and τ depend on both Δw and Δu [21]. In many studies, the CZM is considered as a conventional means to represent non-linear fracture phenomena. Consequently, simplified shapes e.g., linear, bilinear, trapezoidal, exponential, etc. are simply assumed for the cohesive laws[87, 59, 13].

2.2.3 Elastic-interface models

Elastic-interface models constitute a special class of CZMs, where the interaction between the separating sub-laminates is described by linearly elastic traction-separation laws. Accordingly, the delaminated laminate can be regarded as composed of sub-laminates partly connected to each other by a continuous distribution of linearly elasticbrittle springs. This modelling approach dates to the pioneering work by [43], who modelled the double cantilever beam test by considering each arm of the specimen as a beam on an elastic foundation. Elastic-interface models for the analysis of delamination of composite laminates were introduced in the 1990s [20, 2, 27, 3, 65] and later adopted by many Authors [19, 66, 9, 79, 10, 11, 32, 13]. Elastic-interface models have the advantage that the underlying simplifying assumptions enable in many cases the determination of closed-form solutions. Conversely, the predictions of such models are in good agreement with experimental data only for materials exhibiting elasticbrittle behavior or if the analysis is limited to the initiation not propagation of delamination cracks.

2.2.4 Buckling-driven delamination

In composite structures, delaminations can be situated within the bulk or near the surface. When delaminations do not create slender sub-laminates, they can be analyzed by using classical facture mechanics. However, when a delamination is near the surface, so that it creates a slender sub-laminate, the problem must be analysed not only from a fracture mechanics point of view, but also buckling must be taken into account. Such a delamination crack may propagate due to local buckling and the consequent high interlaminar stresses produced at the crack front. Moreover, local buckling and crack propagation may promote a global instability of structural components, such us columns, plates and shells under compression [15].

One of the first works on delamination promoted by buckling is a study by Kachanov [42]. Kachanov studied a fibre-glass composite tube with a surface delamination, subjected to an external pressure (Figure 10).

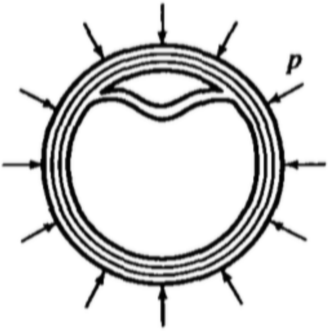

Figure 10: Kachanov's problem of the compressed laminate tube [42]

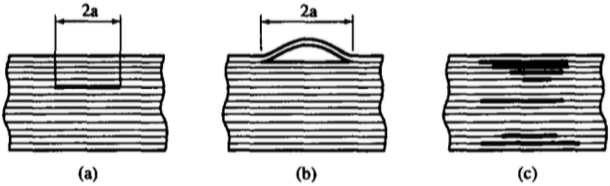

Figure 11: Three types of delaminations: (a) internal, (b) near-surface and (c) multiple cracking [15]

When a delamination involves superficial layers of structural components, its behaviour - under compression or under surface heating - is often charactereized by instability. Sometimes, due to Poisson's effect, some layer may buckle under tension. Bolotin poposed a classification of near-surface delaminations [15](Figure 12).

An important work, that is probably the starting point in the Western literature of studies on delamination promoted by buckling was published by Chai *et al.* [24], where the *thin film model* (*TFM*) and the *thick column model* (*TCM*) were introduced Figure 13.

Among the initial studies, also the simple model must be cited of a plate with a throught the width delamination, loaded with a uniform load in compression by Witcom and Bottega [86, 17]. Suddenly, models began to be more complicated, and a review of the first works on

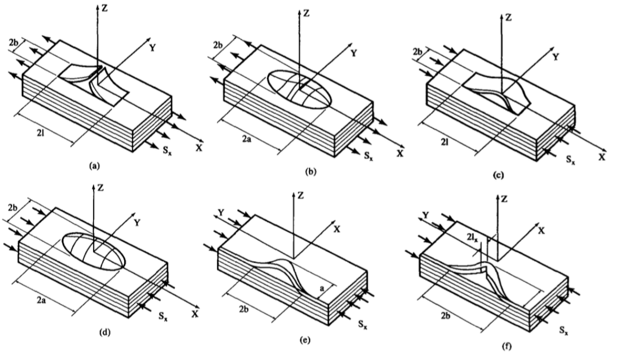

Figure 12: Near-surface delaminations: (a) open delamination in tension; (b) closed one in tension; (c) buckled delamination; (d) closed buckled one; (e) edge buckled delamination; (f) the same with a secondary crack [15]

the topic was done by Storakers [76]. Gradually, the complexity of the models was increased: multiple delaminations and contact between sublaminates were considered citegiannakopoulos1995contact. Tay [82] underlines that it is important to take contact into account when antisymmetric buckling mode may occur (Figure 14); and thermodynamic effects were taken into account by Yin [92].

Buckling driven delamination was studied also for shells, in particular for cylindrical shells [70, 74, 46, 16, 25, 73]. A lot of studies were conducted on the dynamical delamination propagation [71, 26, 91, 57]. In composites delamination, a crucial role also is played by cyclic loads [14, 30, 47, 45].

Besides analytical solutions, numerical methods have been used to study delamination problems. Some authors have adopted the Rayleigh-Riz method [61, 37]. Many authors prefer using the finite element method (FEM) [68, 60, 90, 5] because it can address complex laminate configurations and various boundary conditions.

Senthil *et al.* [72] note that the delamination promoted by buckling is an open problem and there are a lot of different buckling modes that could affect the laminated product (Figure 15). Senthil *et al.* [72] point

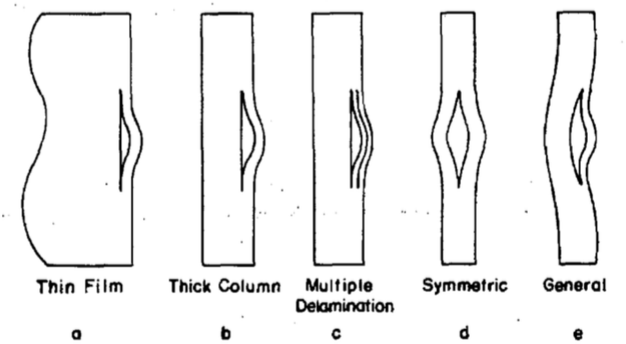

Figure 13: Delamination/buckling models [24]

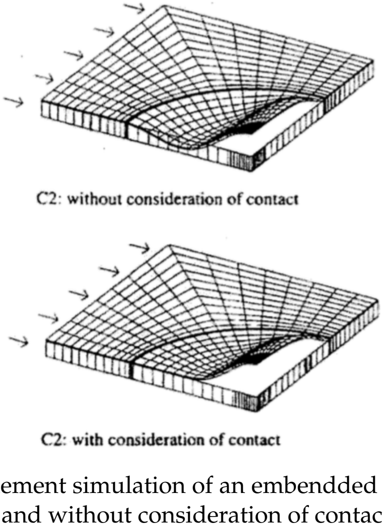

Figure 14: Finite element simulation of an embendded delamination under compression, with and without consideration of contact [82]

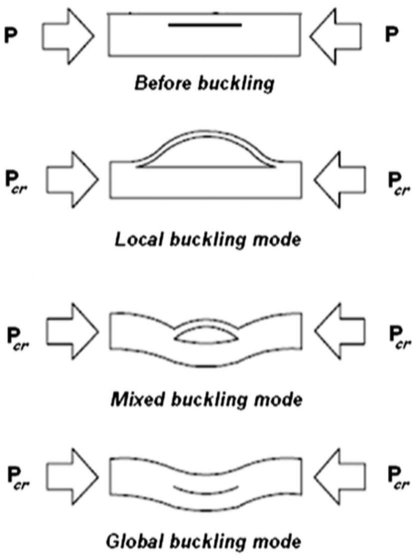

Figure 15: Buckling modes of a composite panel under in-plane compression [72]

Figure 16: Physically inadmissible buckling mode [72]

out that it is also important to exclude physically inadmissible buckling modes when an unconstrained analysis is performed (Figure 16).

Nowadays, buckling driven delamination in composite is still an open problem and many authors investigate on this research topic [69, 51]. To investigate this phenomenon, some authors have suggested carrying out four-point bending tests on composite laminated specimens with mid-span, through-the-width delamination cracks [44, 48, 39, 4].

2.3 Buckling-driven delamination in four-point bending tests

2.3.1 Introduction

In the following section we analyze, in chronological order, some theoretical and experimental studies related to delamination promoted by local buckling in composite laminates subjected to four-point bending tests. When the superficial layer is loaded in compression, the regions where bonding is weak or missing may undergo local buckling. As a consequence, high stresses arise at the contour of the debonded region, thus promoting its further expansion. In Figure 17, we can observe a laminated specimen which contains a pass through delamination, which is subject to four-point bending. The delaminated portion in this configuration, is loaded under compression.

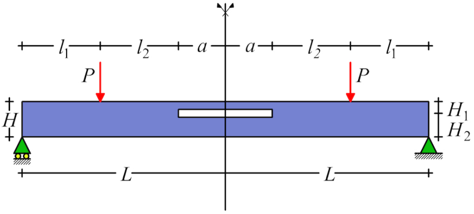

Figure 17: Test specimen

2.3.2 Snap buckling of delaminated composites under pure bending (Kardomateas, 1990)

Introduction

One of the first studies related to delamination promoted by local buckling in composites laminates subjected to bending was conducted by Kardomateas [44]. The Author proposed a mechanical model based on an energetic approach to predict the onset of delamination. He then illustrated some experimental results that turned out to be in good agreement with his theoretical model.

Mechanical model

Kardomateas considered the beam portion reported in Figure 18. He observed that in the upper sub-laminate, the pure bending load produces a compressive axial force equal in magnitude to the tensile axial force acting in the lower sub-laminate.

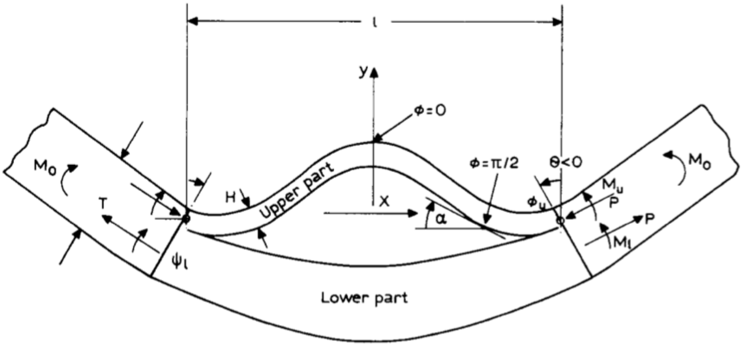

Figure 18: Kardomateas' model [44]

The upper sub-laminate subject to axial compression may buckle after reaching a critical value of the load. Due to the buckling phenomenon, an opening of the crack faces occurs at the two delamination fronts. Then, depending on the applied bending load, the onset and growth of the delamination crack may follow. Kardomateas noticed that the upper sub-laminate is not directly loaded by a uniform compression, but is indirectly loaded in compression due to bending. In fact, the positive bending moment promotes a preferential direction where the sublaminates tends to buckle, but buckling in this direction is impeded by the lower sub-laminate. As a consequence, a new equilibrium configuration will be achieved by snap-buckling.

The Author, using an energetic approach, analyzes an orthotropic laminated beam-plate of unit width and thickness T containing a passing delamination at a height $H(H < T/2)$ from the extrados of the laminate. As we can see in Figure 18, the delamination extends for a portion x between -$l/2$ and $l/2$. In snap-buckling instability, the energy criterion is widely used. In fact, in a transition from one equilibrium configuration to another, the total potential energy changes from a higher value to a lower one. The smallest load value, which produces this passage from a higher energy level to a lower one, corresponds to the critical load. The total potential energy after snap-buckling is:

$$U_{tot} = U_u + \frac{P_u^2 l(1 - \nu_{13}\nu_{31})}{2EH} + U_l + \frac{P_l^2 l(1 - \nu_{13}\nu_{31})}{2E(T - H)} \tag{2.1}$$

where U_u e U_l are respectively the bending contributions of the upper and lower sub-laminates, and the second and fourth terms of the second member are the extensional contributions (P_u and P_l are the axial force of the upper and lower sub-laminates, respectively; T is the thickness of the integer laminate; H is the thickness of the upper sub-laminate; E is the Young's modulus and ν is the Poisson's ratio).

The total potential energy of a beam segment subject to bending, but not buckled, of equal length, is:

$$U_0 = 6M_0^2 l \frac{(1 - \nu_{13}\nu_{31})}{2ET^3} \tag{2.2}$$

The Author imposes the condition $U_{tot} \leq U_0$, together with equilibrium considerations, and arrives at a non-linear system of equations, which provides the critical load.

Discussion of results and comparison with the theoretical model

The experimental studies were carried out on a laminate made up of 15 unidirectional Kevlar 49 pre-impregnated sheets with the following characteristics: nominal thickness of the sheets 0.20 mm; modul of elasticity in the material principal reference: $E_1 = 75.8$ GPa, $E_2 = 5.5$ GPa, $G_{12} = 2.1$ GPa; Poisson's ratio $\nu_{12} = 0.34$.

A through-the-width delamination, with a length of $l = 50.8$ mm,

Table 1: Buckling moment comparison between theory and experiments [44]

H/T	M_{0cr} (Nm) from theory	M_{0cr} (Nm) from tests
$1/15$	0.45	0.30
$3/15$	5.03	4.50
$4/15$	10.46	9.80

was introduced with a Teflon strip of thickness 0.025 mm in the middle section of the specimen. Three specimens were created with delaminations placed at different depths from the extrados, resulting in different values of the $\frac{H}{T}$ ratio (Table 1).

The specimens had a length of 152.4 mm, the distance between the external supports and the points of application of the loads was 25.4 mm and the distance between the two loads was 63.5 mm. The four-point bending test was conducted with a 9 ton servo-hydraulic machine. The deflection was controlled with advances of 0.2 mm/s. An electric resistance strain gauge was placed at the extrados of the delaminated layer to evaluate the buckling moment, which corresponds to the inversion of sign detected by the strain gauge (Figure 19).

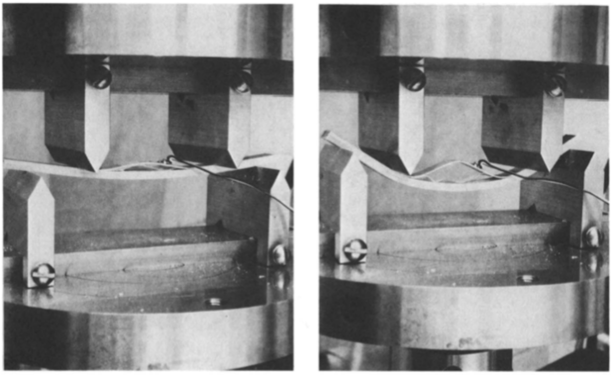

Figure 19: Four-point bending test [44]

In figure 20, we can observe the trends of the applied bending moment and strain at the extrados of the delaminated layer, as functions of the transverse displacement of the load application points. The dashed line represents the buckling moment predicted by the analytical solution.

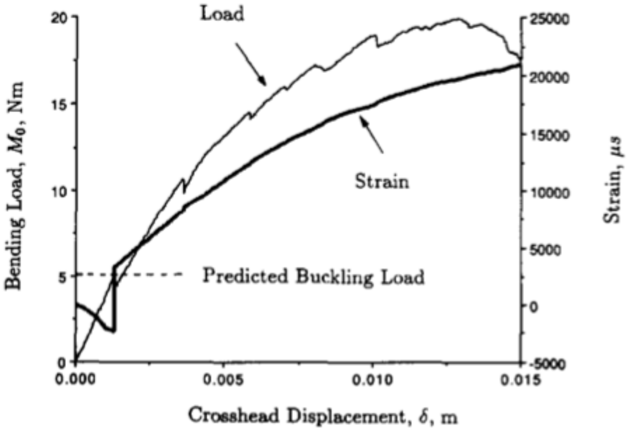

Figure 20: Applied bending moment and strain at the extrados of the delaminated layer, as functions of the transverse displacement of the load application points [44]

2.3.3 Buckling and propagation of a delaminated composite beam in bending (Kinawy, Butler, Hunt, 2010, 2011, 2012)

Introduction

Kinawy, Butler, and Hunt [48, 49, 50] analyzed the snap-buckling problem and the post-critical behavior of a thin sub-laminate of a beam subject to constant bending. They formulated a theoretical model that describes the behavior of the upper sub-laminate that snaps from the closed to open position, compared to the lower sub-laminate. Their model is based on the Rayleigh-Ritz method, whereas approximated analytical expressions are assumed for the deflected centrelines and then the minimum potential energy principle is applied to find the post-buckling response. The Authors obtained a lower limit for the critical bending moment for buckling and crack propagation. The authors also analyzed the fatigue behavior taking into account both the snap-buckling and the propagation moment of the crack tip. In addition, they conducted experimental studies to verify the analytical results.

Analytical model

The Authors propose an analytical model, where they assume that the beam has an isotropic behavior and neglect the non delaminated regions. The delaminated parts are modeled as flexible and extensible beams. The rotation at the end, between the delaminated region and the unbroken regions of the specimen, is assumed equal for each sub-laminate. In addition, it is assumed that there is no relative sliding between the laminates at the interface. The model is described through three degrees of freedom: the rotation at the ends Q_2, the shortening of the ends of the sub-laminates with respect to the delaminated area Δ, and the distance between the intrados of the upper laminate and the extrados of the lower one, Q_1. Figure 21 shows a scheme of the model.

The expressions of the transverse displacements of the deformed centerlines, respectively for the upper and lower laminate, are assumed as follows:

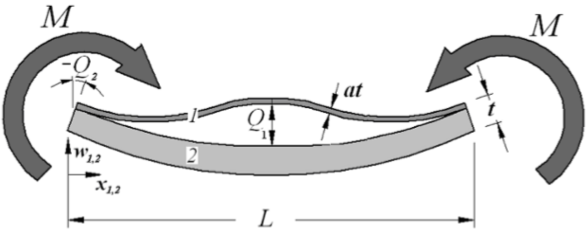

Figure 21: Debonded region, coordinates system and degree of freedom [50]

$$w_1 = Q_1 \sin^2\left(\frac{\pi x_1}{L}\right) + Q_2 \frac{x_1(L - x_1)}{L} \tag{2.3}$$

$$w_2 = Q_2 \frac{x_2(L - x_1)}{L} \tag{2.4}$$

The initial imperfection, introduced with the PTFE foil to create the delaminated region, is schematized with the following function:

$$w_i = Q_i \sin^2\left(\frac{\pi x_i}{L}\right) \tag{2.5}$$

The strain energy is computed by taking into account the extensional and bending contributes:

$$U_B = \frac{EI_1}{2} \int_0^L \left(\frac{d^2(w_1 - w_i)}{dx_1^2}\right) dx_1 + \frac{EI_2}{2} \int_0^L \left(\frac{d^2 w_2}{dx_2^2}\right) dx_2 \tag{2.6}$$

$$U_S = \frac{t}{2L}\left(Ea\delta_1^2 + E(1-a)\delta_2^2\right) \tag{2.7}$$

where δ_1 e δ_2 are the axial shortenings of the upper and the lower sublaminate, respectively.

The total potential energy of the system is:

$$V = U_B + U_S - 2MQ_2 \tag{2.8}$$

The authors solve the equation $\frac{\partial V(Q_1,Q_2,\Delta,M)}{\partial \Delta} = 0$ with respect to Δ and replace the result in V, obtaining a function that depends on Q_1

and Q_2. By solving a suitable system of equations, as indicated in [83], the expressions of Q_1 and Q_2 are obtained as functions of the applied bending moment, M.

Analytical model results

The model was used to predict the buckling moment of a pre - impregnated carbon fiber beam (M21-T800), made of 16 unidirectional layers $[0_{16}]$. It was assumed that the beam had an average thickness of 4.22 mm and a through-the-width delamination placed in the middle-span, 40 mm long, located between the second and third layers. The obtained system of equations was solved by imposing an initial imperfection $Q_0 = 0.02$ mm (Q_0 is the thickness of PTFE layer that was used to create the delamination). The mechanical properties of the material are shown in Table 2. The behavior of the material was assumed as isotropic, whilst the average thickness of each foil was assumed to be 0.26 mm and Young's modulus equal to 155 GPa. Figure 22 shows the trend of the relative displacement Q_1 and the rotation Q_2 of the end as functions of the applied bending moment.

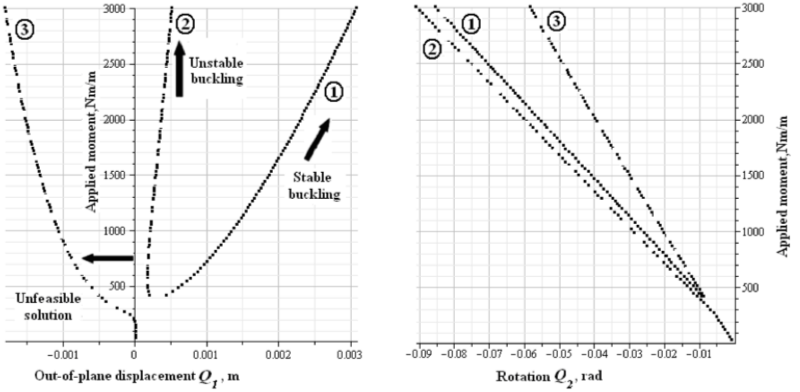

Figure 22: Trend of the relative displacement Q_1 and the rotation Q_2 as functions of the applied bending moment [48]

As we can see in Figure 22, the value of the buckling moment does not

Table 2: Material properties for M21-T800 carbon prepreg [50].

	$E_{11}(GPa)$	$E_{12}(GPa)$	ν_{12}	$G_{12}(GPa)$
Tension	169	8.5	0.33	4.98
Compression	136	9.4	0.33	4.98

appear as a very distinct point. In order to explicitly obtain the critical moment, the authors solved the system for different values of the Q_0 parameter (initial imperfection thickness). They found about 300 Nm/m as the critical moment value, as can be seen in Figure 23.

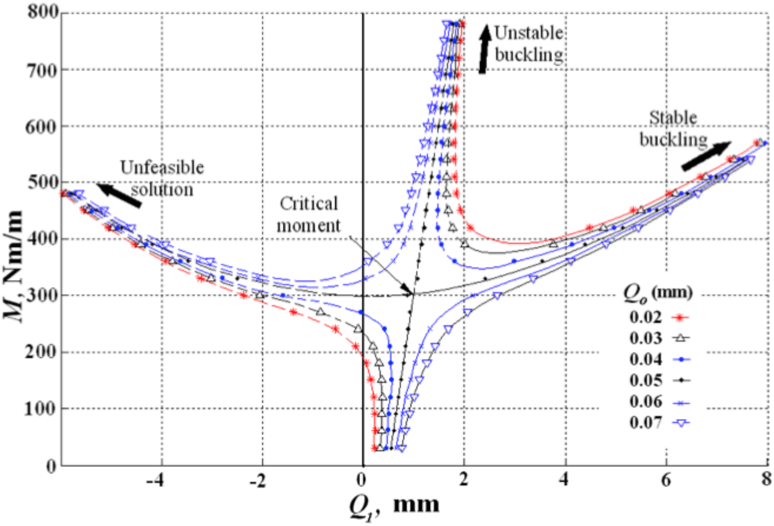

Figure 23: Trend of the relative displacement Q_1 as a function of the applied bending moment, for different values of Q_0 [50]

Authors do not explain why in Figure 23 the bifurcation correspond to a non-null imperfection and curves for $Q_0 < 0.05$ mm approach the bifurcation for increasing value of the imperfection.

Delamination onset

The Authors evaluated the propagation bending moment with the thin film hypothesis assuming crack propagation under pure mode I. They then supposed that the end sections of the thin sub-laminate do not rotate with respect to the thicker sub-laminate. However, their predicted bending moment at crack propagation turned out to be lower than the bending moment reported from static load tests. This suggests that the influence of mode II is important and the accurate prediction of crack propagation requires a mixed mode analysis. The authors calculated the expressions of the energy release rate, G_I and G_{II}, as functions of the stress intensity factors at the crack tip, χ_I and χ_{II}, according to the method proposed by Hutchinson and Suo [40]. They considered a homogeneous and isotropic layer and the force components per unit of width. The stress intensity factors are:

$$\chi_I = \frac{P}{\sqrt{2atU}} \cos(\omega) + \frac{M^*}{\sqrt{2(at)^3U}} \sin(\omega + \gamma) \tag{2.9}$$

$$\chi_{II} = \frac{P}{\sqrt{2atU}} \sin(\omega) - \frac{M^*}{\sqrt{2(at)^3U}} \cos(\omega + \gamma) \tag{2.10}$$

The energy release rate are:

$$G_I = \frac{\chi_I^2}{E} \tag{2.11}$$

$$G_{II} = \frac{\chi_{II}^2}{E} \tag{2.12}$$

where E, P, M^* respectively are the Young's modulus of the material and a linear combination of forces P_1 and the bending moment M_1 e M_2 as show in Figure 24.

Figure 25 shows the trends of the mixed mode index and the mode I and II indices as functions of the applied bending moment. The values of G_{IC} and G_{IIC} were assumed to be 550 and 2700 J/m^2 [64]. We can observe that the contribution of mode I is approximately equal to mode II immediately after the snap-buckling instabilities. By increasing the

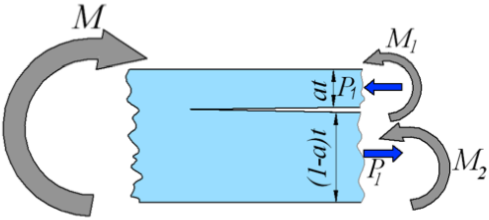

Figure 24: Internal forces at the crack tip [50]

load, the contribution of mode I decreases and the contribution of mode II becomes prevalent.

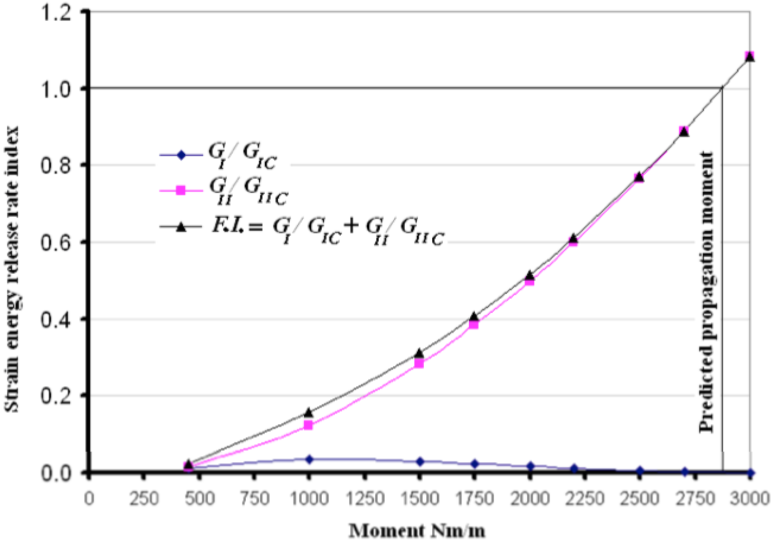

Figure 25: Mode I and II indices as functions of the applied bending moment [50].

Static load tests

The load tests were conducted to evaluate the buckling and delamination propagation behavior. The specimens were laminates made with

16 unidirectional layers. A delamination was introduced by a through-the-width 0.02 mm PTFE layer placed in the middle-span. The specimen dimensions were: $220 \times W \times t$ mm, where W and t are shown in Table 3. An INSTRON-1332 servo-hydraulic machine was used, with a 10 kN load cell. The specimens were subjected to four-point bending tests, controlling the displacement (Figure 26).

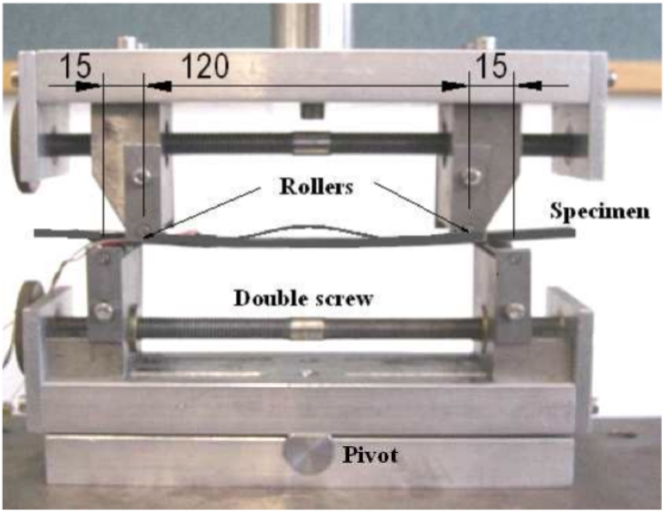

Figure 26: Four-point bending test: experimental setup[48, 49, 50]

Each specimen was equipped with electrical strain gauges placed at the intrados and extrados of the middle-span cross section. The buckling of the upper sublaminate was detected as corresponding to the inversion of the sign of axial strains on the upper sub-laminate. Figure 27 shows the values of the deformations at the extrados and intrados, respectively of the upper and lower sub-laminate as functions of the applied bending moment.

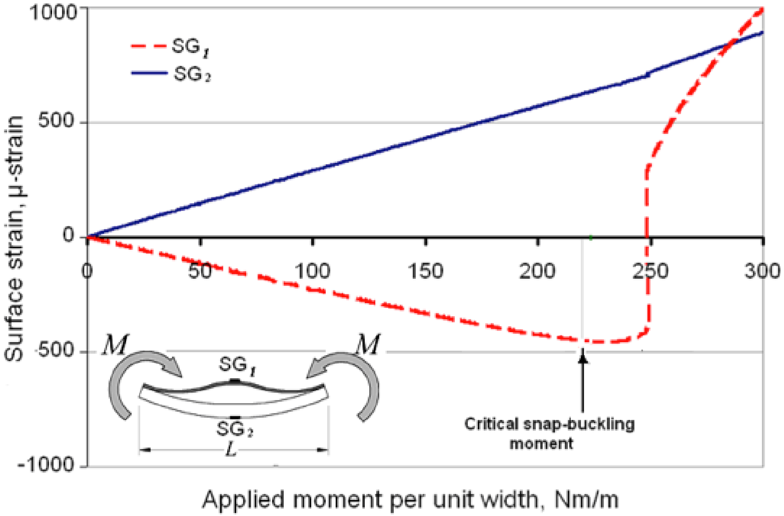

Figure 27: Axial strain at the extrados and intrados, respectively of the upper and lower sub-laminate as functions of the applied bending moment[48]

Table 3 shows the values of the buckling moments for nine specimens. It can observed that the average critical moment is about 270 Nm/m (moment per unit of width).

Table 3: Snap buckling and propagation moments per unit width for tested specimens [50].

Test No.	Width W(mm)	Thickness t (mm)	Snap-buckling moment (Nm/m)	Propagation moment (Nm/m)
1	8.38	4.22	668	2779
2	8.41	4.31	273	2645
3	8.14	4.17	233	2824
4	9.15	4.22	273	2573
5	10.98	4.27	267	2675
6	10.78	4.30	320	2853
7	10.95	4.24	298	–
8	10.94	4.33	261	–
9	11.00	4.22	221	–

The graph in Figure 28 shows the trend of the applied bending moment per unit of width as a function of the displacement of the load application point. Delamination onset occurs when the displacement of the load application point increases and the moment remains constant. The average propagation moment for the nine specimens, as reported in Table 3, is about 2725 Nm / m.

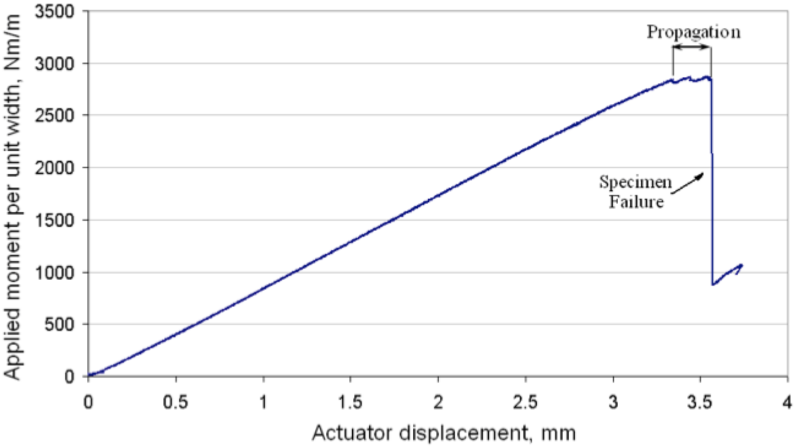

Figure 28: Applied bending moment per unit width as a function of the displacement of the load application point[50]

Fatigue load test

The Authors conducted four-point bending fatigue tests, in order to study the delamination growth varying the applied bending moment. The load ratio R was defined as the ratio between the maximum and minimum applied bending moment during the cycle. For each test, the ratio R was assumed to be 10 and the frequency 4 Hz. The severity was calculated as the ratio between the maximum applied bending moment and the average propagation moment calculated from the static tests. The severity range varied between 0.85 and 0.17, and so the tests always included the range in which the upper sub-laminate becomes unstable. In Figure 29, we can observe the extension of the delaminated area as a function the number of cycles, for different degrees of severity.

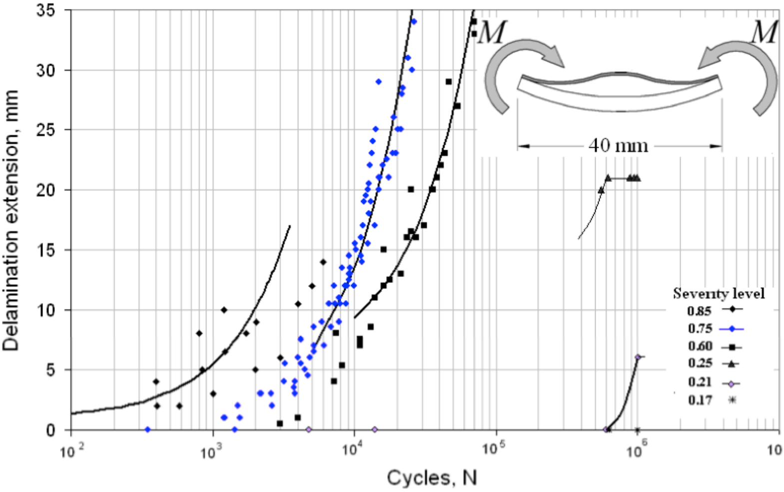

Figure 29: Extension of the delaminated area as a function the number of cycles[50]

2.3.4 Buckling and delamination growth behavior of delaminated composite panels subject to four-point bending (Gong, Chen, Patterson, 2015,2016)

Introduction

Gong, Chen and Patterson [38, 39] experimentally analyzed the stability and growth of the delamination of a laminated panel, containing a low-speed impact delamination, subject to a four-point bending test. They used the Digital Image Correlation (DIC) method to measure the field deformation of the specimen. The effects were assessed on both circular and elliptical delaminations. Finally, they created a numerical model based on the finite element method (FEM) and compared its theoretical predictions with the experimental results. Recently, an analogous approach was adopted by [4].

Four-point bending test

Laminated specimens of 260 mm ×25mm size were made from pre - impregnated carbon fiber MTM57 / T700 (Umeco, Heanor, UK) containing 38% of resin. The stacking sequence was [0/ /90/0/90/0/90/0/90/0/90 /0]°, where the symbol // indicates the position of the delamination. The upper face of the specimens was painted with a thin layer of white paint, then small black spots were sprayed on the white surface in order to have a good contrast during the DIC. The delamination was placed in the middle-span, so the area of interest was focussed on the center line for a length of approximately 50 mm. The specimen was subjected to a four-point bending test, in displacement control with the rate 0.1 mm/min, using a servo-hydraulic machine (*Instron 8501, Instron, UK*) with a load cell of 100 kN. The deformations of the specimen were measured using the 3D DIC (*Q-400, Dantec Dynamics, Germany*). Two cameras were mounted at the top of both sides of the specimen, as shown in Figure 30, with an inclination of 90 degrees to each other, so that the accuracy of the measurement out of plane is the same as that in the plane [78]. Before starting the test, a calibration of the cameras was performed on a 30 mm specimen provided by Dantec Dynamic.

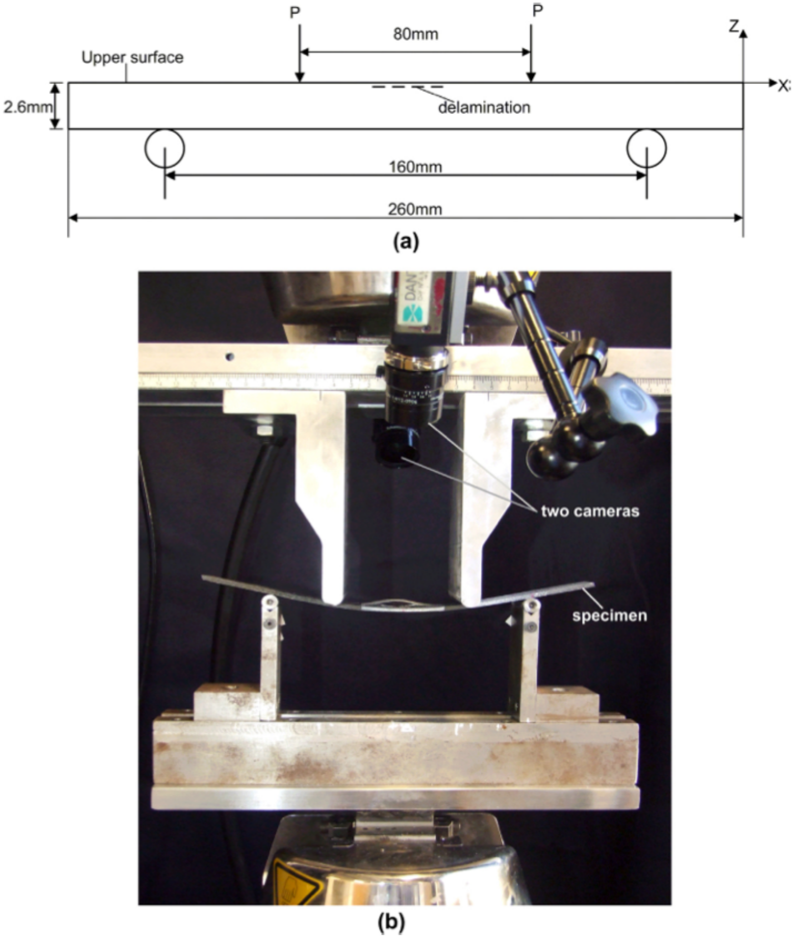

Figure 30: Four-point bending test [38]

Results

The authors [38, 39] tested to failure a specimen containing a 12 mm diameter delamination. Figure 31 shows the trend of the displacement out of the plane of the upper sub-laminate as a function of the applied bending moment. The load path is divided into several sections: initially, until the load has reached the M_A value, the whole specimen behaves like a monolithic beam and bends normally, with downwards displacement; and once the buckling moment value is reached, M_B suddenly jumps upwards; the other jumps at points C, D, E and F correspond to the growth of delamination; once the value of the maximum moment M_G is reached, the crack propagates stably.

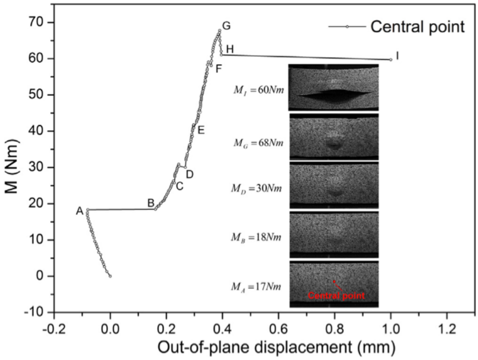

Figure 31: Out-of-plane displacement of the upper sub-laminate as a function of the applied bending moment [38]

Gong, Chen and Patterson analyzed the influence of the form of the delamination crack on both the buckling behavior and crack propagation. They considered circular and elliptical delaminations; the latter sometimes arranged with the major axis in the longitudinal direction and other times in the traversal direction of the specimen. In Figures 32 and 33, we can observe the trend of the bending moment as a function of the out-of-plane displacement of the central point of the specimen, respectively for elliptical delaminations with the major semi-axis placed along the specimen's longitudinal and transverse directions. The Authors note that when the shape of the delamination is circular, the growth of the crack, which appears first in the transverse direction, is governed by buckling. Later, by increasing the load, the crack develops in the longitudinal direction. For elliptical delamination cracks, the growth is always in the longitudinal direction. The Authors note that longitudinal elliptical delaminations are potentially more dangerous, since the critical behavior occurs at lower load values.

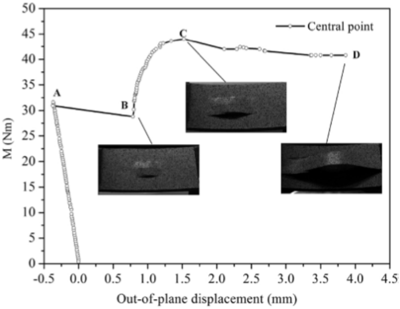

Figure 32: Applied bending moment as a function of the out of plane displacement of the central point of the specimen for elliptical longitudinal delamination [38]

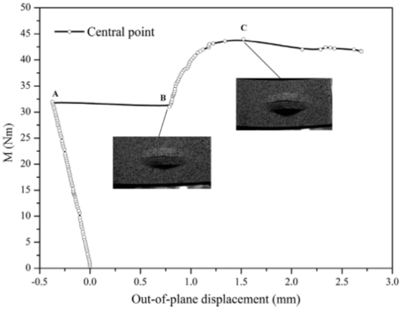

Figure 33: Applied bending moment as a function of the out of plane displacement of the central point of the specimen for elliptical transversal delamination [38]

Finite element analysis

The Authors also developed a non-linear numerical simulation, using the finite element method implemented within the ABAQUS software (Figure 34). In the simulation, a mixed-mode delamination growth criterion proposed by Camanho *et al.* [31] was implemented. The results obtained were compared, in terms of out-of-plane displacement, with those obtained in the experiments (Figure 35).

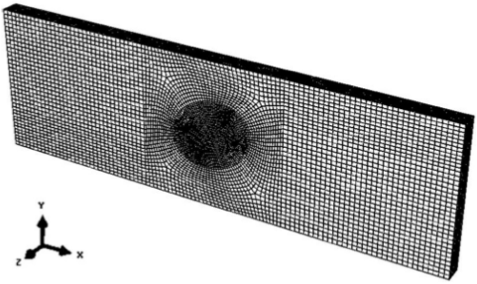

Figure 34: Finite element model [39]

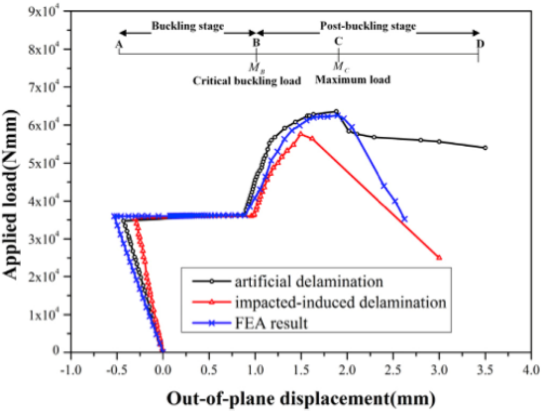

Figure 35: Applied bending moment versus out of plane displacement, experimental and FEM [39]

2.3.5 An elastic-interface model for buckling-driven delamination growth in four-point bending tests (Bennati, Dardano and Valvo, 2017)

Introduction

In [12], we presented a model to describe delamination promoted by local buckling in a composite specimen with a central, through-the-width delamination, subjected to a four-point bending test. The specimen was modeled as an assemblage of sublaminates. Thanks to the symmetry, the analysis was limited to the left-hand half of the specimen, which is subdivided into three zones: a first zone, between the support and the load application point, where the specimen is schematized as a single laminate; a second zone, between the load application point and the delamination front, where the specimen consists of two sub-laminates connected by the elastic interface; and a third zone, between the delamination front and the symmetry axis, where the two previous sub-laminates are no long connected by the interface.

All sub-laminates are considered as extensible and flexible beams undergoing small elastic deformations, except for the compressed sub - laminate in the third zone, which may undergo large displacements. The mechanical problem is described by a set of differential equations with suitable boundary conditions. In the post-critical stage, the energy release rate and mode mixity are evaluated to predict the load corresponding to the onset of delamination growth. The theoretical predictions of the model are in good agreement with some experimental results found within the literature.

Mechanical model

The test specimen is $2L$ long, it has cross-section height H, and width B. The specimen contains a longitudinal delamination of length $2a$ placed at the mid-span cross section. The delamination subdivides the laminates into two sub-laminates of height H_1 and H_2, respectively. The specimen is loaded by two load P in a symmetrical configuration and distant l_1 from the supports and l_2 from the crack front. Thanks to the symmetry, our attention is focused only to the left half of the specimen (Figure 36). The model was divided into three zones with different behavior: a first zone of length l_1, between the support and the load application point, were the laminate is modeled as a single sub-laminate ①; a second zone of length l_2, between the load application point and the delamination crack tip, in which the laminate is schematized as two sub-laminates ② and ③ connected by an elastic interface; lastly, a third zone of length a, where the laminate consists of two unconnected sub-laminates ④ and ⑤. All sub-laminates are considered as extensible and flexible elastic beams. Sub-laminate ④ is modeled according to Eulers model for beam-columns in compression. The different modeling assumption for sub-laminate ④ is consistent with experimental evidence, showing that this portion of the specimen undergoes compression and eventually buckles under high testing loads. The elastic interface is modeled as a continuous distribution of linearly elastic springs acting in the normal and tangential directions with respect to the interface plane. Let k_y and k_z respectively denote the elastic interface constants in the normal and tangential directions.

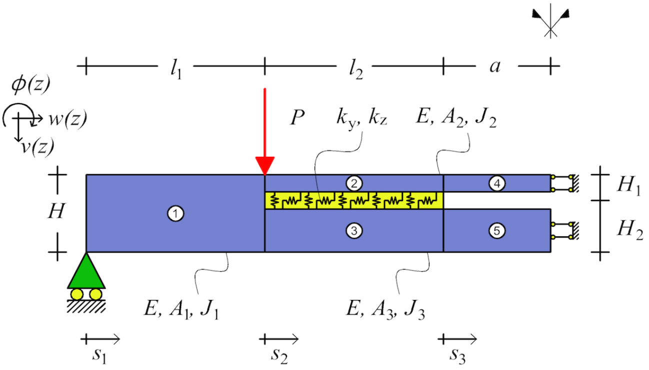

Figure 36: Mechanical model [12]

The governing set of differential equations is the following

$$\begin{cases} EJ_1 v_1^{IV}(z) = 0; \\ EA_1 w_1^{II}(z) = 0 \\ EJ_2 v_2^{IV}(z) - Bk_y(v_3(z) - v_2(z)) - \frac{1}{2} H_1 EA_2 w_2^{III}(z) = 0 \\ EA_2 w_2^{II}(z) = Bk_z(w_3(z) - w_2(z) + \frac{1}{2} H_2 v_3^{I}(z) + \frac{1}{2} H_1 v_2^{I}(z) \\ EJ_3 v_3^{IV}(z) + Bk_y(v_3(z) - v_2(z)) + \frac{1}{2} H_1 EA_3 w_3^{III}(z) = 0 \\ EA_3 w_3^{II}(z) = -Bk_z(w_3(z) - w_2(z) + \frac{1}{2} H_2 v_3^{I}(z) + \frac{1}{2} H_1 v_2^{I}(z) \\ EJ_2 v_4^{IV} = \begin{cases} 0 \text{ in pre-critical stage;} \\ -P_4 v_4^{II} \text{ in post-critical stage;} \end{cases} \\ EA_2 w_4^{II}(z) = 0; \\ EJ_3 v_5^{IV}(z) = 0; \\ EA_3 w_5^{II}(z) = 0; \end{cases} \tag{2.13}$$

Completed by the boundary conditions:

$$\begin{cases} v_1(0) = 0;\ M_1(0) = 0;\ N_1(0) = 0; \\ v_1(l_1) = v_2(0);\ v_1(l_1) = v_3(0);\ \phi_1(l_1) = \phi_2(0);\ \phi_1(l_1) = \phi_3(0); \\ M_1(l_1) = M_2(0) + M_3(0) - \frac{1}{2} H_2 N_2(0) + \frac{1}{2} H_1 N_2(0); \\ T_1(l_1) - P = T_2(0) + T_3(0);\ w_1(l_1) - \dfrac{1}{2} H_2 \phi_1(l_1) = w_2(0); \\ w_1(l_1) + \dfrac{1}{2} H_1 \phi_1(l_1) = w_3(0);\ N_1(l_1) = N_2(0) + N_3(0); \\ v_2(l_2) = v_4(0);\ \phi_2(l_2) = \phi_4(0);\ M_2(l_2) = M_4(0);\ T_2(l_2) = T_4(0); \\ w_2(l_2) = w_4(0);\ N_2(l_2) = N_4(0);\ v_3(l_2) = v_5(0);\ \phi_3(l_2) = \phi_5(0); \\ M_3(l_2) = M_5(0);\ T_3(l_2) = T_5(0);\ w_3(l_2) = w_5(0);\ N_3(l_2) = N_5(0); \\ \phi_4(a) = 0;\ T_4(a) = 0;\ w_4(a) = 0; \\ \phi_5(a) = 0;\ T_5(a) = 0;\ w_5(a) = 0 \end{cases} \tag{2.14}$$

Analytical model results

After solving the previous system of equation, we determined the trend of the applied bending moment vs. the relative displacement between the sub-laminates ④ and ⑤, $\Delta v(a)$, at the mid-span cross section (Figure 37). Moreover, to better understand all paths, we print the deformed shape for each path and eliminate all unfeasible solution paths. In Figure 37, we compare our analytical model with the experimental resultus of Kinawy *et al.* [48, 49, 50]. In the post-critical stage, we expect a progressive increase in the interfacial stresses, eventually leading to further growth of the delamination crack. Since both normal and tangential stresses are present at the crack tips, fracture will occur under I/II mixed-mode conditions. To predict the onset of delamination growth, we first evaluate the energy release rate and mode mixity. Then, we compare the available energy release rate with the critical value according to the criterion of Hutchinson and Suo [40]. From the beginning, this model presents numerical instabilities due to the elastic interface, and it was very difficult to estimate k_y and k_z. Starting from this paper, we implement a new mechanical model that is reported in chapter 5.

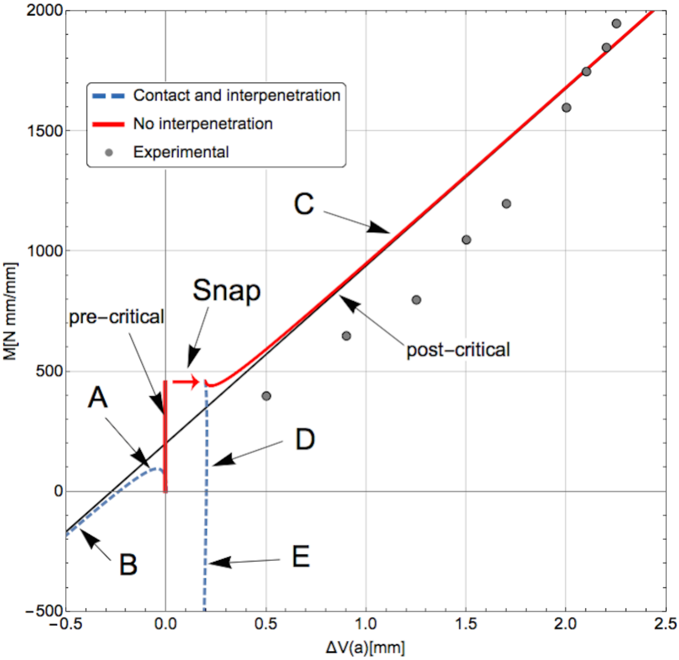

Figure 37: Predicted response and experimental data [12]

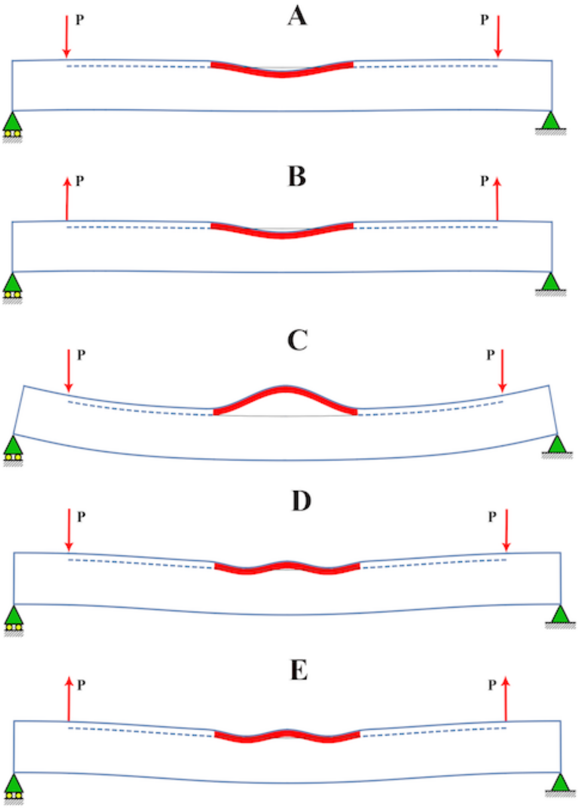

Figure 38: Deformed configurations of the specimen for each solution path [12]

Chapter 3

Experimental interface characterization

3.1 Introduction

The four-point bending tests conducted fot the PhD thesis were obtained from a laminated plate manufactured using quasi-unidirectional carbon-fibre fabric and epoxy resin. The Manufacturer, Microtex Composites S.r.l., Prato, provided us the longitudinal Young's modulus and mode I interlaminar fracture toughness, but the mode II interlaminar fracture toughness was unknown. Therefore, as explained in this chapter, the mode II fracture toughness was evaluated by carrying out at MUSAM Lab same prelimirary end-notched flexural (ENF) tests according to the ASTM standard [29].

3.2 Mode I fracture toughness

The longitudinal Young's modulus and mode I interlaminar fracture toughness communicated by the Manufacturer are listed in Table 4 and reported in Figure 39.

Table 4: Mechanical properties of the unidirectional carbon fibre-reinforced laminate used in the experimental tests

$E[GPa]$	$G_{IC}[J/m^2]$
129.5	812

3.3 Mode II fracture toughness

3.3.1 ENF tests

A laminated plate (300 mm × 400 mm) was manufactured having a total of 16 plies and a nominal thickness of 5.2 mm. Six 220 mm × 25 mm specimens were cut from the plate to conduct end-notched flexural (ENF) tests according to the ASTM standard [29]. A 50 mm long artificial delamination was created at the end of each specimen (the delamination position was marked by a white mark as shown in Figure 40) by introducing a thin layer of polytetrafluoroethylene (PTFE) between the eighth and ninth plies.

Prior to the final delamination tests, each specimen was pre - cracked through a preliminary ENF test aimed at producing a sharp crack tip. Then, the position of the new crack tip was observed and marked by using an optical microscope available at the Section of Aerospace Engineering of the Department of Civil and Industrial Engineering of the University of Pisa. Finally, the delamination tests were conducted at the Multiscale Analysis of Materials Laboratory (MUSAM-Lab) at IMT School for Advanced Studies, Lucca. A Zwick-Roell universal testing machine with 10 kN load cell was used under displacement control with a rate of 0.5 mm/min.

3.3.2 Compliance calibration

According to [29], a calibration procedure was adopted to evaluate the specimen compliance. Each specimen was loaded in a three point bending test, with 100 mm span length and different crack lengths, until the

50% of the expected failure load was reached. In particular, tests were conducted for delamination lengths equal to 20, 25, 35, and 40 mm. At the end, a failure test with 30 mm crack length was carried out to evaluate the critical load for mode II delamination. Figure 42 shows the load vs. displacement plots obtained from the tests for each specimen.
All of the experimental curves feature an initial non-linear response, probably due to the deformability of the test fixture. So, according to [29], the portions of the curves between 0 and 300 N were discarded and only the values in the range between 300 and 700 N were used to evaluate the compliance. According to [29], the compliance calibration factors, A and m, were obtained using a linear list square linear regression analysis with the compliance, C, versus cubed crack length (a^3) as the following polynomial expression:

$$C = A + ma^3$$

where A is the intercept and m is the slope obtained from the regression analysis.

Figure 43 illustrates the compliance fitting for each specimen. Figure 44 reports a comparison among the compliance calibration curves.

3.4 Results

Mode II fracture toughness was evaluated as

$$G_{IIc} = \frac{3m}{2B} P_{max}^2 a_0^2 \tag{3.1}$$

were m is the coefficient of the interpolating polynomial, B is the specimen width, P_{max} is the mode II fracture propagation load (assumed as the maximum load recorded in experiments), and $a_0 = 30$ mm is the initial delamination length. Table 5 reports the values obtained of G_{IIc}, P_{max}, and m for each specimen, as well as their mean value and standard deviation. The mean value obtained for G_{IIc} will be used later to predict the onset of delamination in four-point bending tests.

Table 5: Experimental values of G_{IIc}, P_{max}, and m for each specimen

	$G_{IIC}[J/m^2]$	$P_{max}[N]$	$m[N^{-1}m^{-2}]$
Specimen 1	2015.4	1743.5	0.0125
Specimen 2	1951.1	1848.4	0.0106
Specimen 3	2113.0	1829.6	0.0117
Specimen 4	1997.4	1818.5	0.0112
Specimen 5	1781.2	1796.7	0.0103
Specimen 6	2012.7	1839.3	0.0111
Mean value	**1978.5**	**1811.2**	**0.0112**
Standard deviation	**110.1**	**41.6**	**7.8771** $\times 10^{-4}$

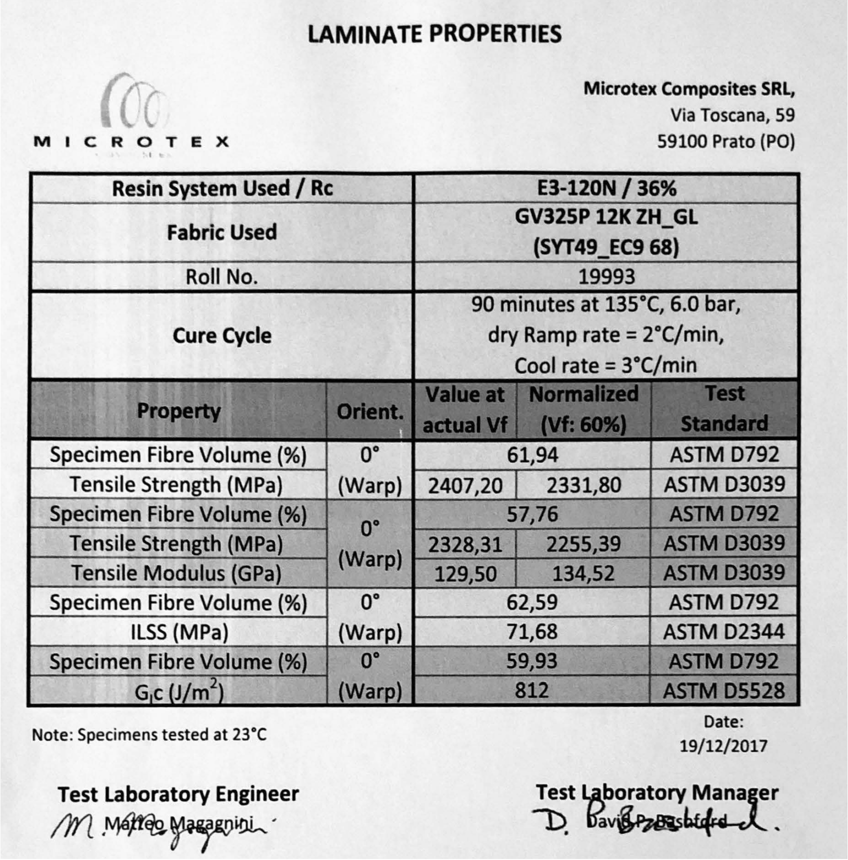

LAMINATE PROPERTIES

MICROTEX

Microtex Composites SRL,
Via Toscana, 59
59100 Prato (PO)

Resin System Used / Rc	**E3-120N / 36%**
Fabric Used	**GV325P 12K ZH_GL (SYT49_EC9 68)**
Roll No.	19993
Cure Cycle	90 minutes at 135°C, 6.0 bar, dry Ramp rate = 2°C/min, Cool rate = 3°C/min

Property	**Orient.**	**Value at actual Vf**	**Normalized (Vf: 60%)**	**Test Standard**
Specimen Fibre Volume (%)	0° (Warp)	61,94		ASTM D792
Tensile Strength (MPa)		2407,20	2331,80	ASTM D3039
Specimen Fibre Volume (%)	0° (Warp)	57,76		ASTM D792
Tensile Strength (MPa)		2328,31	2255,39	ASTM D3039
Tensile Modulus (GPa)		129,50	134,52	ASTM D3039
Specimen Fibre Volume (%)	0° (Warp)	62,59		ASTM D792
ILSS (MPa)		71,68		ASTM D2344
Specimen Fibre Volume (%)	0° (Warp)	59,93		ASTM D792
G_{Ic} (J/m^2)		812		ASTM D5528

Note: Specimens tested at 23°C

Date:
19/12/2017

Test Laboratory Engineer
Matteo Magagnini

Test Laboratory Manager
David P. Bashford

Figure 39: Microtex Composites S.r.l. specifications

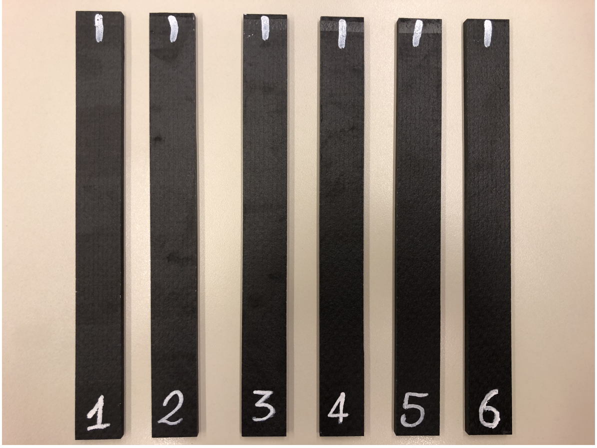

Figure 40: Specimens.

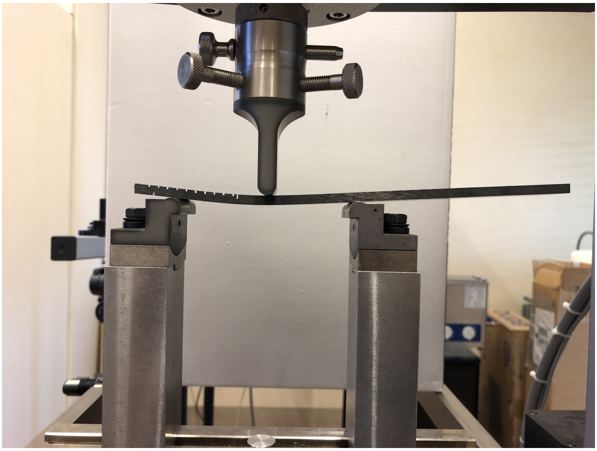

Figure 41: ENF test.

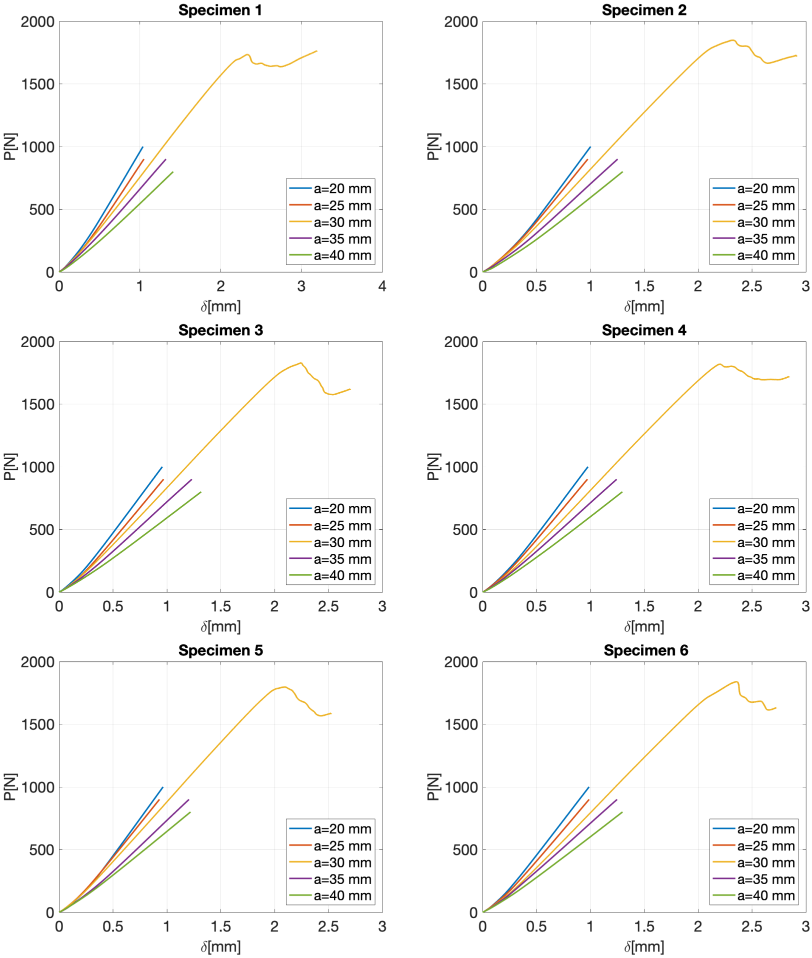

Figure 42: Compliance calibration and delamination toughness tests on each specimen

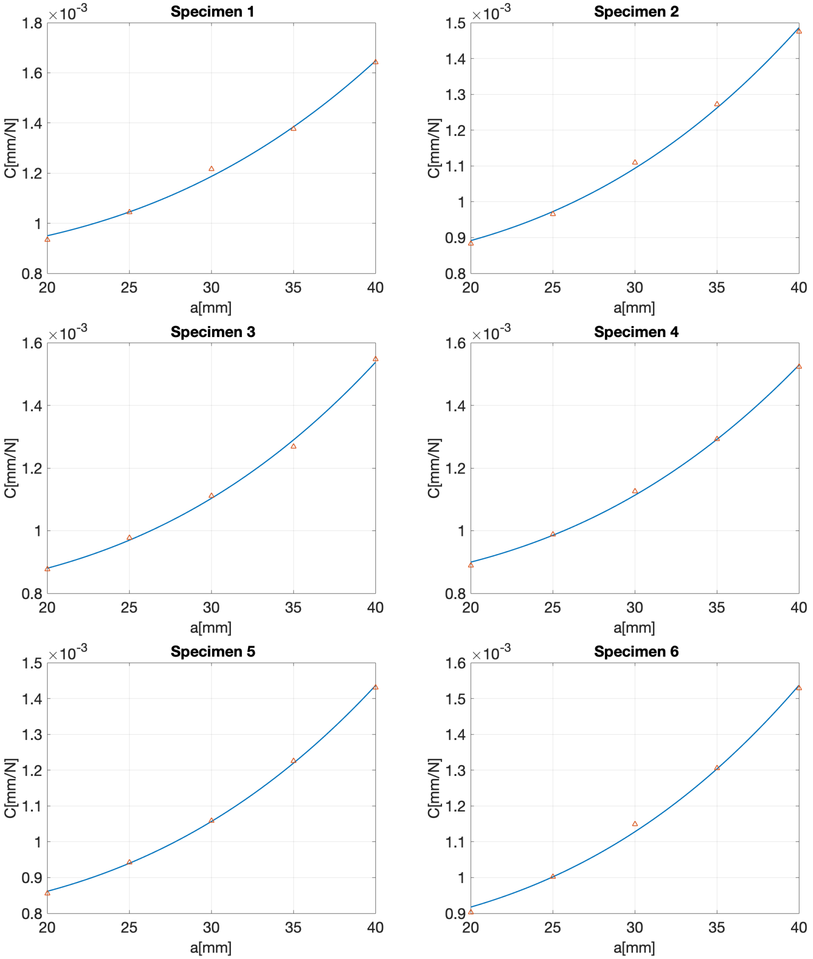
Specimen 1

Specimen 2

Specimen 3

Specimen 4

Specimen 5

Specimen 6

Figure 43: Compliance calibration curves for each specimen

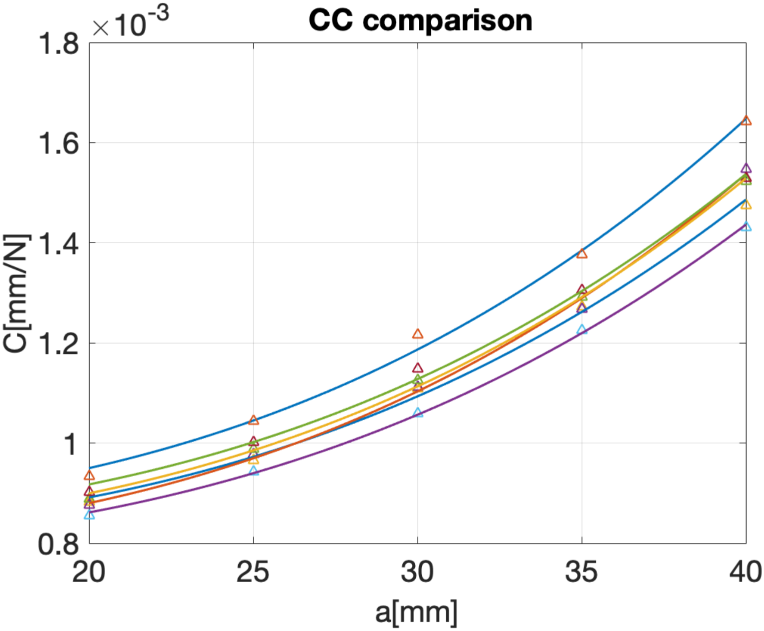

Figure 44: Comparison among compliance calibration curves.

Chapter 4

Four-point bending tests

4.1 Introduction

To study buckling - driven delamination, experimental tests were conducted on delaminated specimens. The specimens were subjected to four-point static bending tests by using the universal testing Machine Zwick/Roell and the Digital Image Correlation facilities available at IMT MUSAM Lab. This type of test is standardized, but only for monolithic specimens, by the ASTM D7264/D7264M-15 [29]. However, we referred to this rule to the extent it was also applicable in the case of delaminated samples. In order to obtain the information necessary to compare experimental results with a theoretical model, during our experiments we measured the applied load and the corresponding displacements. Furthermore, the crack length and the crack opening of the delaminated area were measured by using a Digital Image Correlation technique.

4.2 Specimens

4.2.1 Design

The specimens was designed as reported in Figure 45.

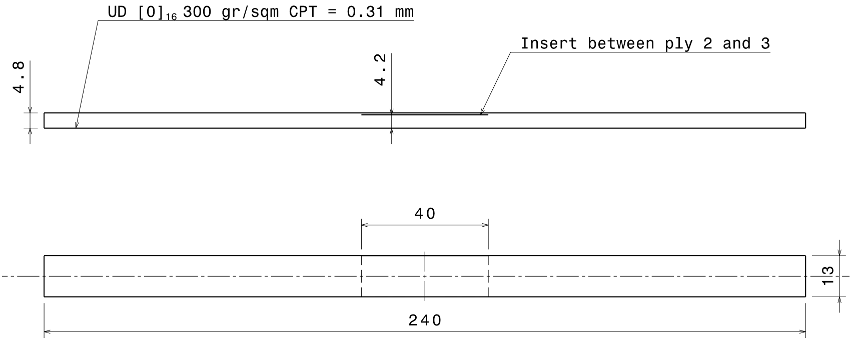

Figure 45: Artificial delamination

4.2.2 Manufacturing

Specimens were produced by Microtex Composites S.r.l., a 300 mm× 400 mm laminated plate was manufactured using quasi-unidirectional carbon-fibre fabric GV325P 12KZH_ GL(SYT49_ EC968) with an epoxy resin content of 36%. The plate had a total of 16 plies and a nominal thickness of 5.1 mm. Ten 220 mm× 13 mm specimens were cut from the plate to conduct Four-Point Bending Test (FPBT) according to the ASTM standard [28].

The specimens were subjected to a cure cycle for 90 minutes at a temperature of 135°C, at 6 bar pressure. The curing temperature was reached with a dry ramp rate of $2°C/min$. The laminate was cooled with a $3°C/min$. The slow heating rate of the specimen give the possibility to the epoxy resin to penetrate into the carbon fabric. The cure cycle influences the final thickness of specimens; the above mentioned cycle produces a 5.1 mm thick laminate, 0.9 mm thicker than the designed one.

A 40 mm long artificial delamination was created at the middle-span of each specimen by introducing a thin layer of polytetrafluoroethylene (PTFE) between the second and third plies. To avoid edge effect, the specimens were cut by a water jet from the original plate.

4.2.3 Preparation

At IMT MUSAM Lab, prior to the buckling-driven delamination tests, each specimen was numbered and measured as reported in Table 6 . Each debonded portion was pre-opened by a needle to eliminate any residual glue (Figure 58).

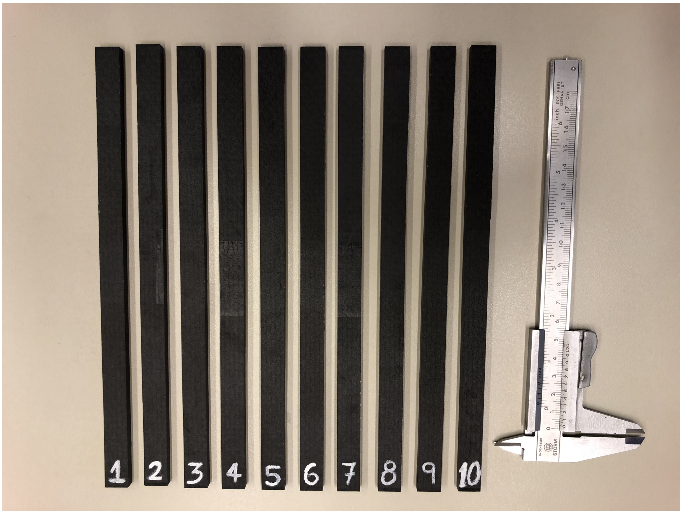

Figure 46: Four-point bending specimens

Table 6: Geometrical dimensions of specimens

N	lenght [mm]	thickness [mm]	width [mm]
0	238.00	5.20	13.00
1	238.00	5.20	12.93
2	238.00	5.27	12.87
3	238.00	5.22	12.92
4	238.00	5.35	12.78
5	238.00	5.20	12.93
6	238.00	5.27	12.88
7	238.00	5.30	12.88
8	238.00	5.28	12.90
9	238.00	5.30	12.90
10	238.00	5.38	12.77
mean	238,00	5.26	12.89
Dev St %	0	5.02	6.62

Furthermore, full field displacement was measured with the Digital Image Correlation (DIC). Each side of the specimens was prepared by using a random black speckled pattern with a spray paint (Figure 47).

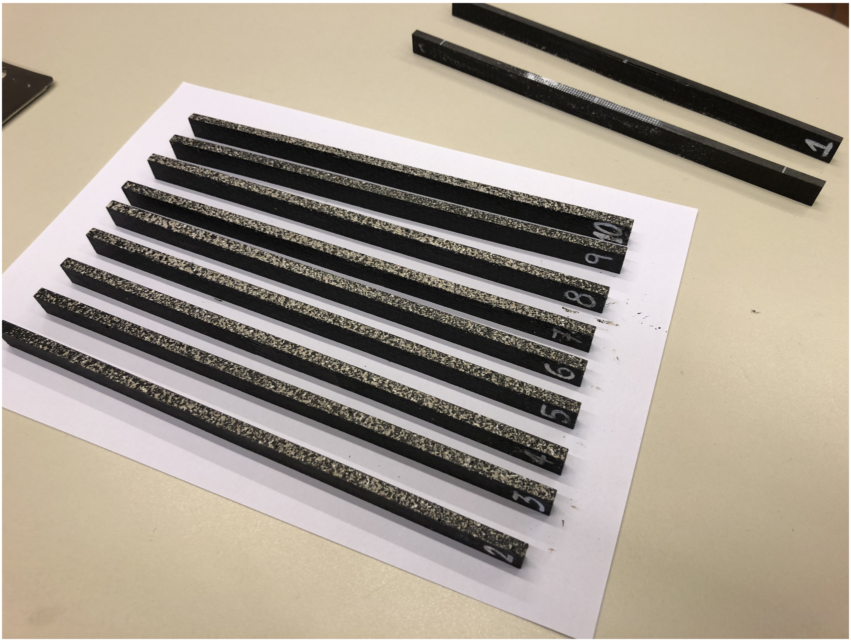

Figure 47: Specimen preparation with a black pattern paint

4.3 Four-point bending tests

4.3.1 Testing machine

The specimens were subjected to a four point bending tests by using a Zwick-Roell universal testing machine with 10 kN load cell under displacement control with a rate of $0.5mm/min$. The spacing between the upper knives was set at 10 cm, and the spacing of the lower knives was set at 20 cm, as reported in Figure 48 and according to the ASTM standard [28]. The centre of the debonded region was placed symmetrical to the the middle span cross section.

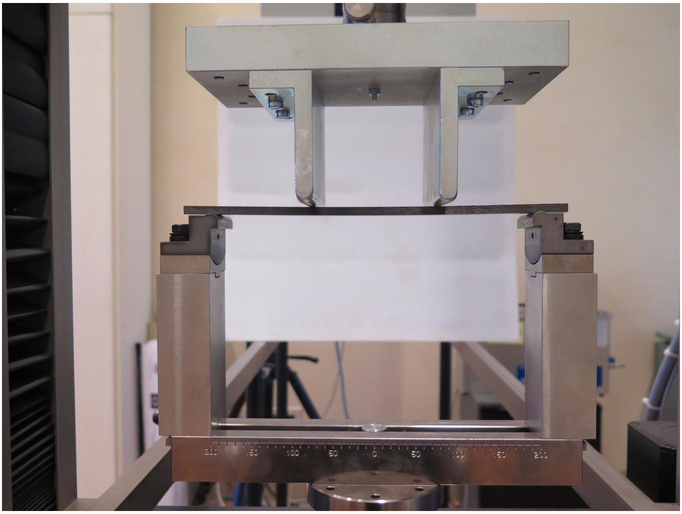

Figure 48: Crossbeam displacement vs applied load

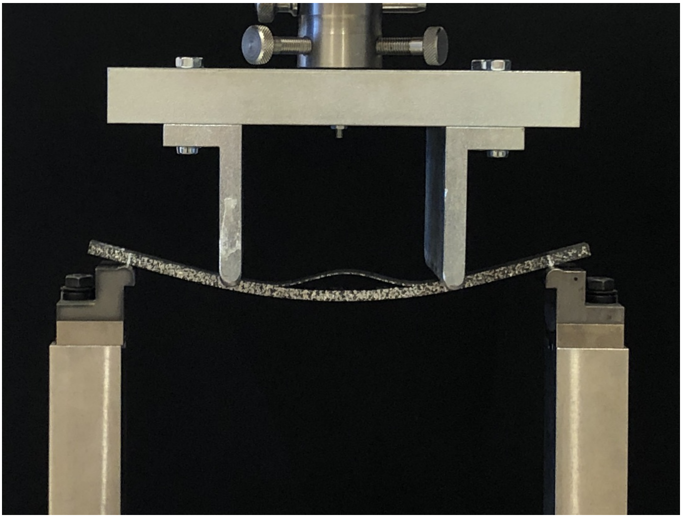

Figure 49: Crossbeam displacement vs applied load

4.3.2 Load jig

To perform the four-point bending test, we designed a load jig to be used with the available testing machine. The pieces were realized in S275 galvanized-steel by Meccanica Precisa S.r.l. Lucca. In Figure 50, the plan of the load jig is shown. The position of the load application knives can be easily changed just by unscrewing the bolts.

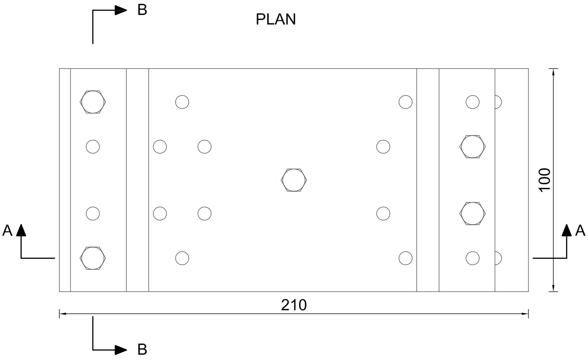

Figure 50: Load jig plan

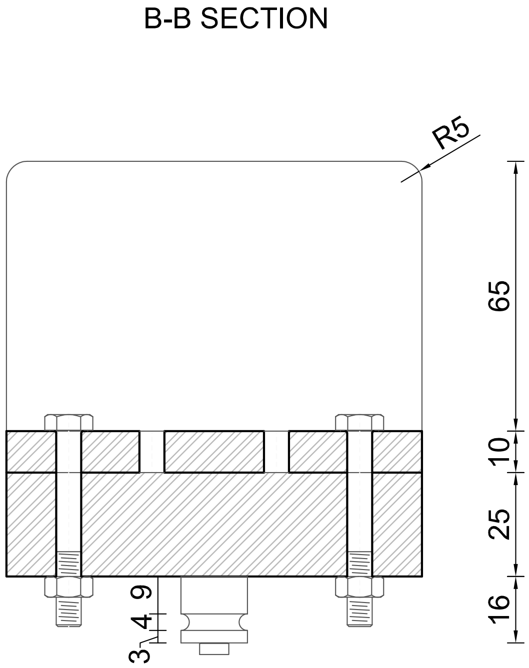

Figure 51: Load jig transverse section

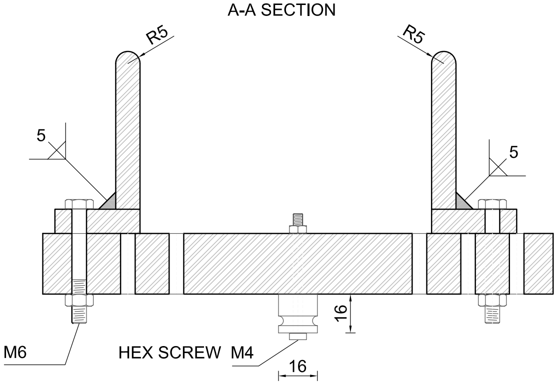

Figure 52: Load jig longitudinal section

4.3.3 Digital Image Correlation

As a recent technology, Digital Image Correlation (DIC) is a non-contact optical technique for measuring strain and displacement fields. The application of DIC to mechanics began during the first years of ’80 [62, 63, 77]. Nowadays is widely used and a recent review on this topic is reported in [58]. The basic idea of DIC, is to compare a sequence of photos of a specimen during the progressive application of a load. The specimens are previously prepared by a random paint film, which allows the user to follow pixels during a deformation stage. The images can be captured by using a common digital camera or a more advanced camera.
A 2D Digital Image Correlation analysis was carried out to measure the full field displacement (Figure 54). We use the Correlated Solution instrument to acquire images with a resolution of 2 Mpixel at a rate of 1photo/second. The camera is reported in Figure 53.

The images were processed by the software *GOM Gmbh* able to identify areas of a measurement image that contain enough image information. In this way, the software can identify the same areas in other measurement images as well. The software can identify the locations of distinct transitions of gray values from black to white based on the gradient. In each distinct gray value transition, the software fits an ellipse. The center point of the ellipse is the measuring point.

Figure 53: Allied Camera

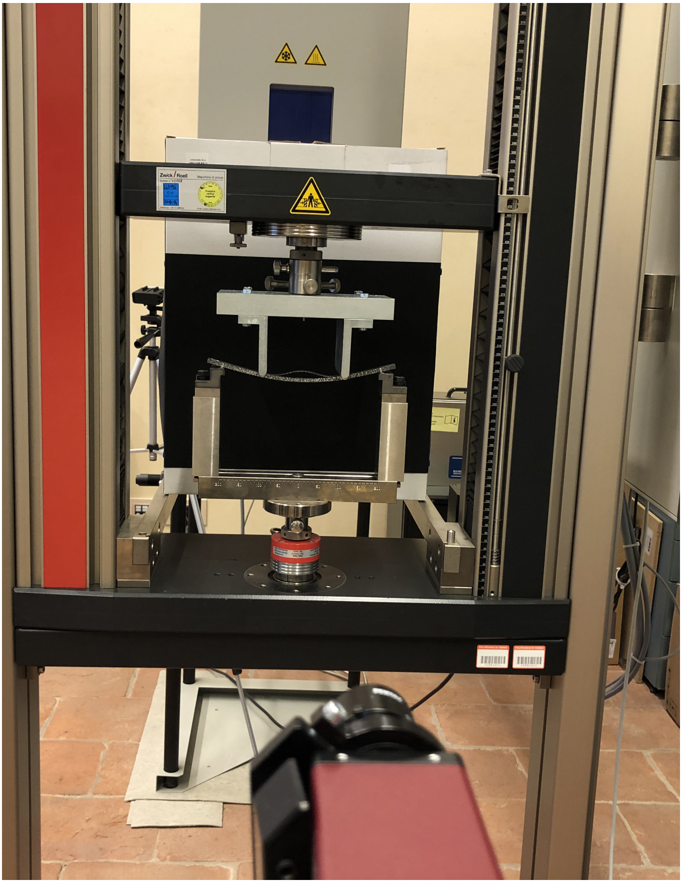

Figure 54: DIC equipment

4.4 Experimental results

4.4.1 Load vs displacement

In Figures 55, 56 and 57, we report the displacement of the crosshead of the testing machine vs. applied load. The tests were carried out with a data acquisition rate of 10 measure/second.

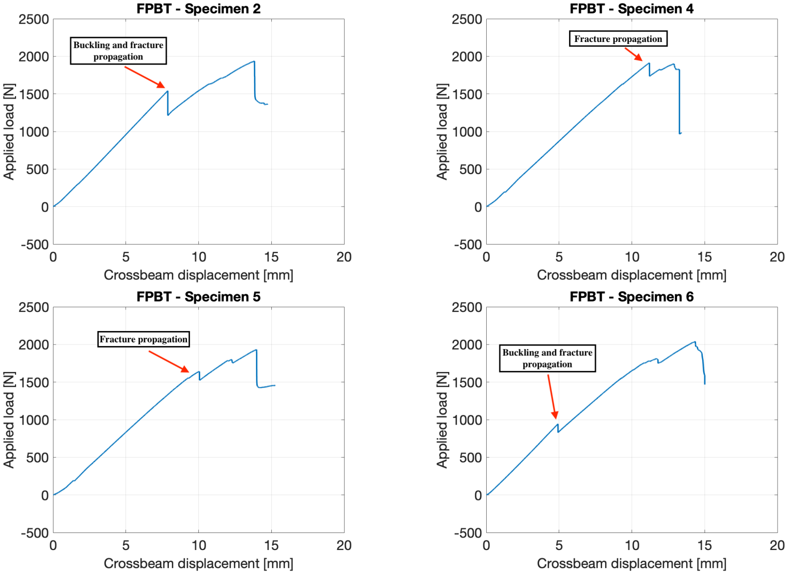

Figure 55: Applied load vs crossbeam displacement for specimen 2, 4, 5 and 6.

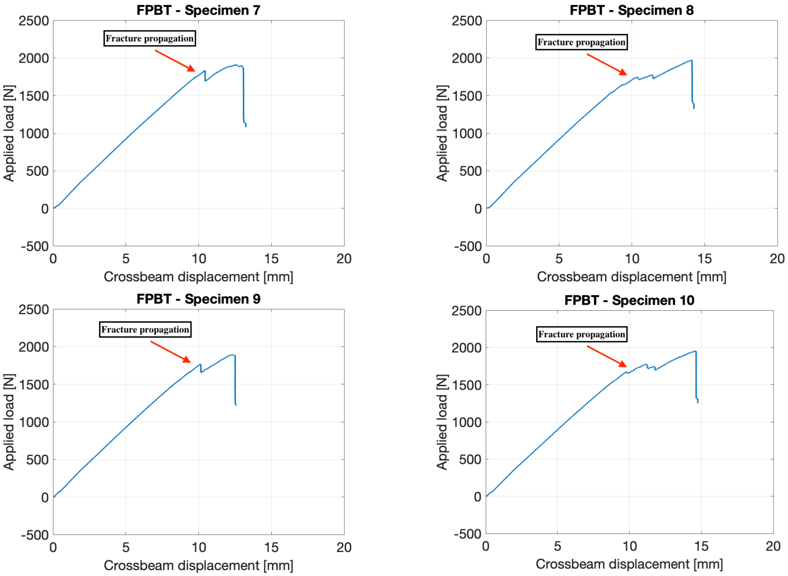

Figure 56: Applied load vs crossbeam displacement for specimen 7, 8, 9 and 10

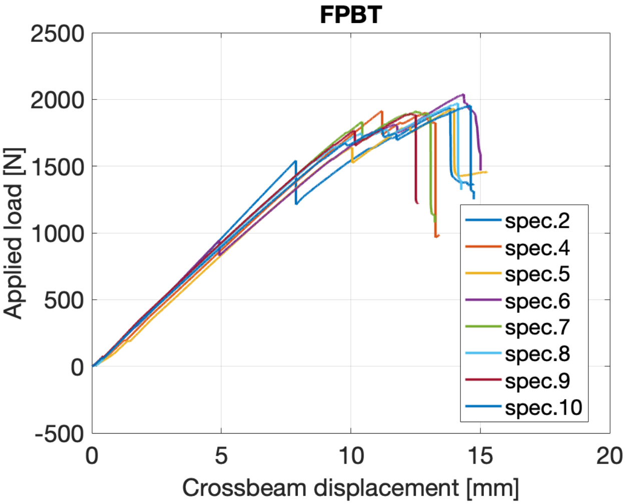

Figure 57: Applied load vs crossbeam displacement for all specimens

Specimen 1 was used to conduct preliminary tests for the final organization of the experimental campaign. At the beginning of our experiments, we tested specimens as they arrived from the manufactures. However, as can be observed in Figure **??**, the behavior of specimen 2 is quite different from the others. In fact, delamination promoted by buckling occurs much earlier than the other specimens. Moreover, specimen 3 broke before snap-buckling occured. Due to these problems, and to have the possibility to observe buckling and delamination separately, we decided to introduce a small imperfection with a 0.63 mm diameter needle in the center cross-section. So, specimens 4, 5, 7, 8, 9 and 10 was tested using this small imperfection, as we can observe in Figure 58.

As witnessed by the graphs in Figure **??**, it is possible to observe a first path were the applied load vs. cross-head displacement is linear. As the load increases and snap-buckling occurs, there is a loss of stiffness due to the buckling of the debonded region. After snap-buckling occurs, it is possible to observe another linear path, with a smaller slope than the first path. Continuing to increase the load, delamination onset occurs and the crack propagates until the crack tip reach the load application point (Figure 59).

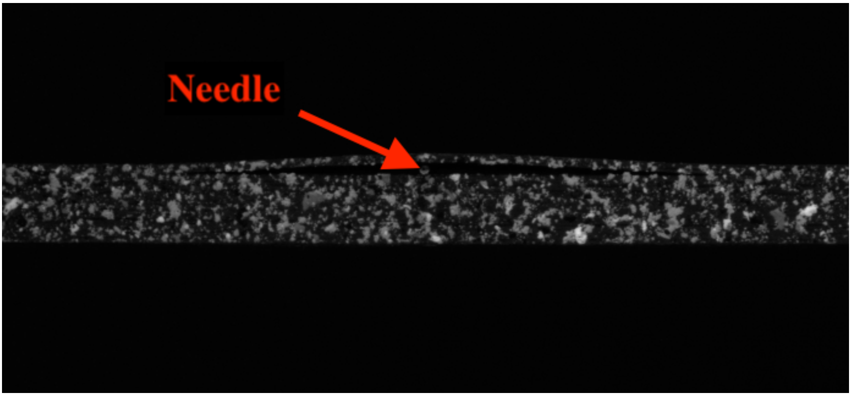

Figure 58: Pre-opened area by introducing a nail of $0.63mm$ diameter into the mid-span

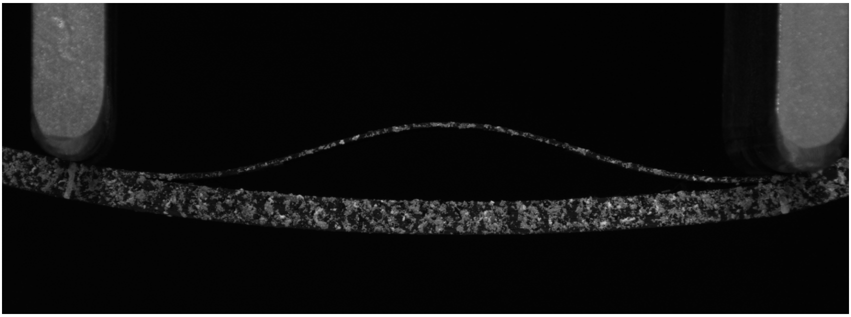

Figure 59: Broken specimen

4.4.2 Crack opening

To measure the crack opening displacement during the test, the Digital Image Correlation (DIC) was used. The acquired photos were processed with software GOM-correlate. The area of interest was focussed on the entire specimen. As a first step, we did a classical DIC, but the displacement field of our specimen was very large. In fact, if we look at the deformed specimen in Figure 49, we can see that the displacement is of the same order of the thickness. The area of interest of the upper sub-laminate was very thin, so at a certain point, during the classical forward DIC, the software loosed the area of interest of the upper sub-laminate. For this reason, we did a backward analysis where the area of interest was set in the deformed configuration. Thanks to this, we were able to measure the relative displacements between the upper and lower sub-laminates.

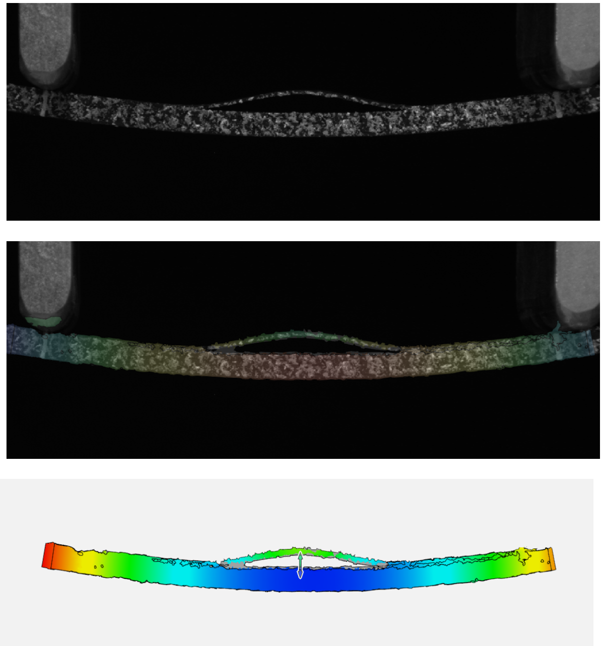

The frame-rate was 1 photo per second, whereas the sampling-rate of the universal testing machine was 10 measure per second. For the above mentioned reason, we synchronized the displacement field and

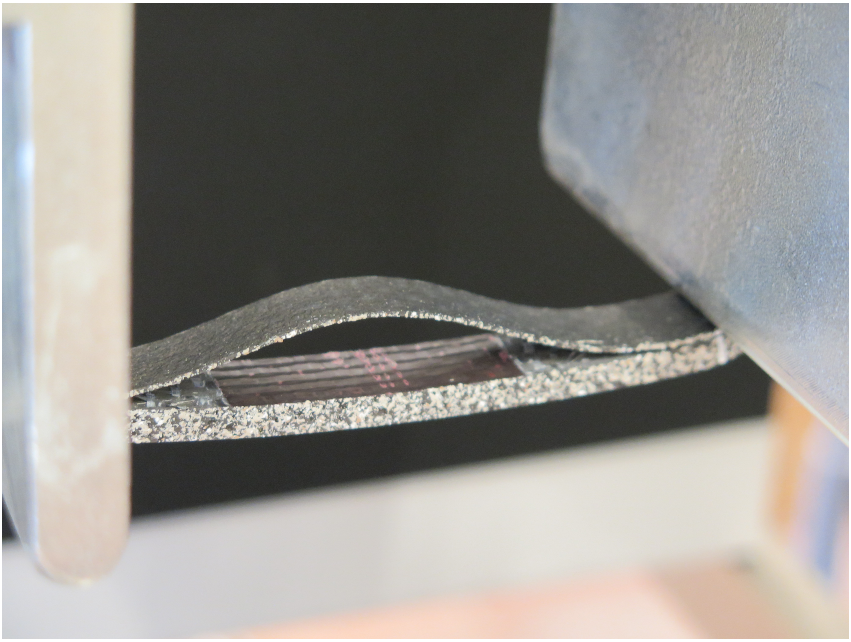

Figure 60: Broken specimen

the load field by eliminating 9 measures for each second from the load acquisition. In Figure 61, we report the applied bending moment versus crack opening, ΔV, measured in the middle-span. As can be observed, the distance between the upper and lower sub-laminates at the middle span is close to zero (or slightly more than zero due to the insertion of the nail) until the load reaches the value of about 500 Nmm/mm. That value corresponds to the snapping moment. After snapping, we can observe a non linear behavior of the specimens until propagation, when ΔV is around 2 mm. The specimens 1, 2 and 3 were not reported here because, as explained in the previous paragraph, specimen 1 was used to set-up the test; in specimen 2 snap-buckling occurred together with unstable delamination; and specimen 3 broke before snap-buckling occurred.

Table 7: Buckling and crack bending moments

Specimen	$M_{buckling}[Nmm/mm]$	$M_{crack}[Nmm/mm]$
4	553.5	2132.8
5	530.5	2404.2
7	529.0	2714.5
8	554.6	2403.2
9	540.3	2389.6
10	454.3	2395.5
Average	527.0	2406.6
Standard dev.	37.3	184.5

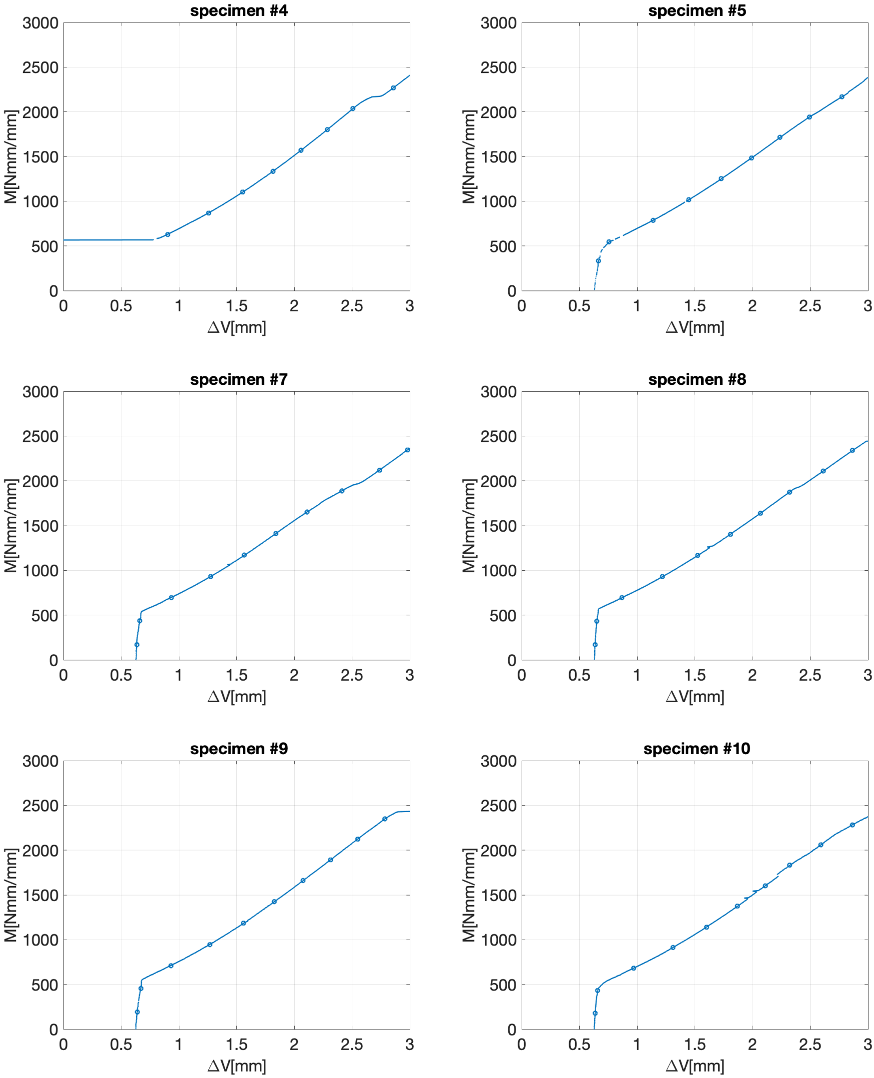

Figure 61: Applied bending moment vs crack opening displacement

Chapter 5

Mechanical model

In this Chapter, a mechanical model of the four-point bending test is developed to interpret the experimental results. Let us consider a laminate of length $2L$, whose cross section has thickness H and width B. A delamination crack of length $2a$ is present at the midspan cross section at distances H_1 and H_2 from the top and bottom surfaces of the laminate, respectively. The laminate is subjected to a four-point bending test with two loads of intensity P, both placed at distances l_1 from the outer supports and l_2 from the delamination crack tips (Figure 62).

The mechanical model considers the specimen as an assemblage of sub-laminates. Due to the symmetry of the problem, it is possible to limit the study to the left-hand half of the specimen by introducing appropriate constraints at the symmetry axis (Figure 62). Unsymmetrical configuration could not be possible due to impossibility of interpenetration of the delaminated zone. In particular, the specimen can be divided into two zones with different behavior: a first zone of length $l_1 + l_2$, between the support and the delamination crack tip, in which the laminate is schematized as a single sub-laminate ①,②; and a second zone, where the laminate consists of two unconnected sub-laminates ③ and ④.

Local abscissas, s_1, s_2, s_3 and s_4 are used in each zone (with $s_3 = s_4$). All sub-laminates are considered as extensible and flexible elastic beams. Sub-laminates ①,② and ③ are modeled according to Euler-

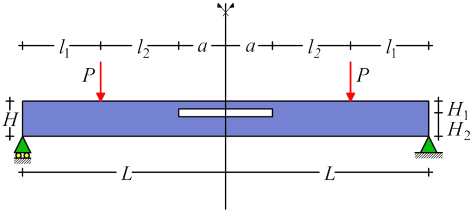

Figure 62: Test specimen

Bernoulli beam theory. Sub-laminate ④ is modeled according to von Kármán beam-plate model. The different modeling assumptions for the sub-laminates are consistent with experimental evidence, showing that only sub-laminate ④ undergoes compression and eventually buckles under high testing loads. Let A_i and J_i $(i = 1, 2, 3, 4)$ respectively denote the area and moment of inertia of sub-laminates (with $A_1 = A_2$ and $J_1 = J_2$). The longitudinal Youngs modulus E is considered constant throughout the specimen.

5.1 Pre-buckling behavior

Before buckling occurs, the specimen behaves as a monolithic specimen without delamination. In fact, the portion between the two applied loads is loaded in pure bending. So, in this portion, the shear stress is equal to zero, as in a monolithic beam. By using the principle of virtual work, we evaluate the diplacement of the load application point versus the applied load, P:

$$V_2(0) = \delta = \int_0^{l_1} \frac{s_1(Ps_1)}{EJ_1} ds_1 + \int_0^{l_2+a} \frac{l_1(Pl_1)}{EJ_1} ds_1 \tag{5.1}$$

$$\delta = \frac{P}{EJ_1} l_1^2 (\frac{1}{3} l_1 + l_2 + a) \tag{5.2}$$

The axial force of sublaminate ④, P_4, is:

$$P_4 = -B \int_{-\frac{H_1+H_2}{2}}^{\frac{H_1-H_2}{2}} \sigma(z)dy = \frac{PBl_1H_1H_2}{2J_1} \tag{5.3}$$

By substituting P_4 into equation 5.2 we obtain the value of the displacement δ as a function of P_4:

$$V_2(0) = \delta = \frac{2P_4l_11(l_1/3 + l_2 + a)}{EBH_1H_2}$$

(5.4)

5.2 Buckling behavior: differential problem

In this section, we report the differential problem for each portion of the specimen. Let v_i, w_i and ϕ_i, respectively denote the transverse and axial displacements, and rotations (positive if clockwise) of a generic cross section.

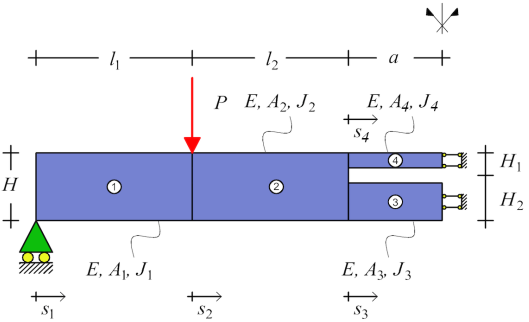

Figure 63: Mechanical model

5.2.1 Portions ①, ②, ③

These three portions of specimen are schematized as classical Euler - Bernoulli beams, so the equations for the transversal and axial displacement for each portions are:

$$EJ_1 v_1^{IV}(s_1) = 0 \tag{5.5}$$

$$EA_1 w_1^{II}(s_1) = 0 \tag{5.6}$$

$$EJ_2 v_2^{IV}(s_2) = 0 \tag{5.7}$$

$$EA_2 w_2^{II}(s_2) = 0 \tag{5.8}$$

$$EJ_3 v_3^{IV}(s_3) = 0 \tag{5.9}$$

$$EA_3 w_3^{II}(s_3) = 0 \tag{5.10}$$

The general solution for each portion one:

$$v_1(s_1) = C_1 s_1^3 + C_2 s_1^2 + C_3 s_1 + C_4 \tag{5.11}$$

$$w_1(s_1) = C_5 s_1 + C_6 \tag{5.12}$$

$$v_2(s_2) = C_7 s_2^3 + C_8 s_2^2 + C_9 s_2 + C_{10} \tag{5.13}$$

$$w_2(s_2) = C_{11} s_2 + C_{12} \tag{5.14}$$

$$v_3(s_3) = C_{13} s_3^3 + C_{14} s_3^2 + C_{15} s_3 + C_{16} \tag{5.15}$$

$$w_3(s_3) = C_{17} s_3 + C_{18} \tag{5.16}$$

where $C_1, C_2, C_3, C_4, C_5, C_6, C_7, C_8, C_9, C_{10}, C_{11}, C_{12}, C_{13}, C_{14}, C_{15}$, C_{16}, C_{17}, C_{18} are constants of integration.

5.2.2 Portion ④

For the sub-laminate ④ we assume a different model. In fact, the specimen is modeled as a von Kármán beam-plate. So, starting from von Kármán strain measures for a plate, here specialized for a beam, we obtain the following strain components: the axial strain

$$\varepsilon_4(s_4) = \frac{\partial w_4}{\partial s_4} + \frac{1}{2}(\frac{\partial v_4}{\partial s_4})^2 \tag{5.17}$$

that could also be obtained from Green-Lagrange strain tensor by considering the axial strain component and neglecting the quadratic term of axial displacement; and the curvature

$$\chi_4(s_4) = -\frac{\partial^2 v_4}{\partial s_4^2} \tag{5.18}$$

Now, by imposing the equilibrium in a deformed configuration and taking into account the constitutive law for the bending moment ($M_4 = EJ_4\chi_4$), we obtain the following differential equations:

$$\begin{cases} EJ_4 v_4^{IV}(s_4) - N_4 v^{II}(s_4) = 0; \\ N_4^I(s_4) = 0 \end{cases} \tag{5.19}$$

From the second equation, we obtain $N_4 = C_{24} = -P_4$, where C_{24} is an integration constant and P_4 is the compressive axial force in sub-laminate ④.

Then, the solution for the transverse displacement becomes:

$$v_4(s_4) = C_{19} + C_{20}s_4 + C_{21}\sin(\lambda_c s_4) + C_{22}cos(\lambda_c s_4); \tag{5.20}$$

where $\lambda_c = \sqrt{\frac{P_4}{EJ_4}}$;

In addition, by recalling the constitutive law for the axial force ($N_4 = EA_4\epsilon_4$), we obtain:

$$N_4(s_4) = EA_4(w_4^I(s_4) + \frac{1}{2}(v_4^I(s_4))^2) \tag{5.21}$$

So, the axial displacement becomes:

$$w_4(s_4) = \frac{C_{24}}{EA_4}s_4 - \frac{1}{2}\int v_4^I(s_4)^2 ds_4 + C_{23} \tag{5.22}$$

where $C_{19}, C_{20}, C_{21}, C_{22}, C_{23}$ are constants of integration. Furthermore, $P_4 = -C_{24}$, the compressive axial load of sub-laminate ④ is a further unknown.

5.2.3 Boundary conditions

The general solution needs to be supported by 24 boundary conditions, which guarantee balance and kinematic compatibility. The solution of the boundary condition system allows for the evaluation of 24 integration constants. The formulated problem describes the behavior of the specimen:

$$\begin{cases}
v_1(0) = 0;\ M_1(0) = 0;\ N_1(0) = 0; \\
v_1(l_1) = v_2(0);\ \phi_1(l_1) = \phi_2(0);\ M_1(l_1) = M_2(0); \\
T_1(l_1) - P = T_2(0);\ w_1(l_1) = w_2(0); N_1(l_1) = N_2(0); \\
w_2(l_2) - \dfrac{H_2}{2}\phi_2(l_2) = w_4(0); \\
w_2(l_2) + \dfrac{H_1}{2}\phi_2(l_2) = w_3(0);\ N_2(l_2) = N_3(0) + N_4(0) \\
v_2(l_2) = v_3(0);\ \phi_2(l_2) = \phi_3(0);\ v_2(l_2) = v_4(0);\ \phi_2(l_2) = \phi_4(0) \\
M_2(l_2) = M_3(0) + M_4(0) - \frac{1}{2}H_2N_4(0) + \frac{1}{2}H_1N_3(0); \\
T_2(l_2) = T_3(0) + T_4(0); \\
\phi_3(a) = 0;\ T_3(a) = 0;\ w_3(a) = 0 \\
\phi_4(a) = 0;\ T_4(a) = 0;\ w_4(a) = 0;
\end{cases} \tag{5.23}$$

5.3 Buckling behavior: solution strategy

5.3.1 Internal forces

By recalling the constitutive laws for beams, the following expressions are deduced for the internal forces in sublaminates:

$$M_1(s_1) = -EJ_1 v_1^{II}(s_1) \tag{5.24}$$

$$T_1(s_1) = -EJ_1 v_1^{III}(s_1) \tag{5.25}$$

$$N_1(s_1) = EA_1 w_1^{I}(s_1) \tag{5.26}$$

$$M_2(s_2) = -EJ_2 v_2^{II}(s_2) \tag{5.27}$$

$$T_2(s_2) = -EJ_2 v_2^{III}(s_2) \tag{5.28}$$

$$N_2(s_2) = EA_2 w_2^{I}(s_2) \tag{5.29}$$

$$M_3(s_3) = -EJ_3 v_3^{II}(s_3) \tag{5.30}$$

$$T_3(s_3) = -EJ_3 v_3^{III}(s_3) \tag{5.31}$$

$$N_3(s_3) = EA_3 w_3^{I}(s_3) \tag{5.32}$$

$$M_4(s_4) = -EJ_4 v_4^{II}(s_4) \tag{5.33}$$

$$T_4(s_4) = -EJ_4 v_4^{III}(s_4) \tag{5.34}$$

$$N_4(s_4) = -P_4 \tag{5.35}$$

By substituting the general expressions obtained for the displacement $v_1(s_1)$, $w_1(s_1)$, $v_2(s_2)$, $w_2(s_2)$, $v_3(s_3)$, $w_3(s_3)$, $v_4(s_4)$, $w_4(s_4)$, we obtain:

$$M_1(s_1) = -EJ_1(6C_1 s_1 + 2C_2) \tag{5.36}$$

$$T_1(s_1) = -EJ_1 6C_1 \tag{5.37}$$

$$N_1(s_1) = EA_1 C_5 \tag{5.38}$$

$$M_2(s_2) = -EJ_2(6C_7 s_2 + 2C_8) \tag{5.39}$$

$$T_2(s_2) = -EJ_2 6C_7 \tag{5.40}$$

$$N_2(s_2) = EA_2 C_{11} \tag{5.41}$$

$$M_3(s_3) = -EJ_3(6C_{13} s_3 + 2C_{15}) \tag{5.42}$$

$$T_3(s_3) = -EJ_3 6C_{13} \tag{5.43}$$

$$N_3(s_3) = EA_3 C_{17} \tag{5.44}$$

$$M_4(s_4) = EJ_4(\lambda_c^2 C_{21} \sin(\lambda_c s_4) + \lambda_c^2 C_{22} cos(\lambda_c s_4)) \tag{5.45}$$

$$T_4(s_4) = EJ_4(\lambda_c^3 C_{21} cos(\lambda_c s_4) - \lambda_c^3 C_{22} sin(\lambda_c s_4)) \tag{5.46}$$

$$N_4(s_4) = C_{24} \tag{5.47}$$

5.3.2 Integration constants

The previous system of equations (5.23) is non-linear, in particular due to the last equation $w_4(a) = 0$. As a solution strategy, we consider the applied load, P, as a complementary unknown and we rebuild the solution as a function of the axial force, $P_4 = -C_{24}$, of the sub-laminate ④. Just by solving the first 23 equations, we obtain the 23 constants of integration:

$$C_1 = \frac{2aJ_4P\lambda_c cos(a\lambda_c) + (2J_3P - aJ_4(2l_2P + HP_4)\lambda_c^2)\sin(a\lambda_c)}{12EJ_1D_1} \tag{5.48}$$

$$C_2 = 0 \tag{5.49}$$

$$\begin{aligned} C_3 = & \frac{1}{4EJ_1D_1}(-2aJ_4l_1(l_1 + 2l_2)P\lambda_c cos(a\lambda_c) + \\ & + (-2l_1(2aJ_1 + J3(l_1 + 2l_2))P)\sin(a\lambda_c) + \\ & + (2aHJ_1P_4 + aJ_4(l_1 + l2)(2l_1l2P + \\ & + H(l_1 + l_2)P_4)\lambda_c^2)\sin(a\lambda_c)) \end{aligned} \tag{5.50}$$

$$C_4 = 0 \tag{5.51}$$

$$C_5 = 0 \tag{5.52}$$

$$C_6 = \frac{1}{4E}\left(\frac{aH_1 sin(a\lambda_c)(HP_4 - 2l_1P)}{D_1} - \frac{4aP_4}{A_3}\right) \tag{5.53}$$

$$C_7 = \frac{aJ_4(2l_1P - HP_4)\lambda_c^2\sin(a\lambda_c)}{12EJ_1D_1} \tag{5.54}$$

$$C_{8=}\frac{l1(2aJ_4P\lambda_c cos(a\lambda_c) + (2J_3P - aJ_4(2l_2P + HP_4)\lambda_c^2)\sin)a\lambda_c))}{4EJ_1D_1} \tag{5.55}$$

$$\begin{aligned} C_9 = {} & \frac{-4aJ_4l_1l_2P\lambda_c cos(a\lambda_c) + (-4l_1(aJ_1 + J_3l_2)P)\sin(a\lambda_c)}{4EJ_1D_1} + \\ & + \frac{(2aHJ_1P_4 + aJ_4l_2(2l_1l_2P + H(2l_1 + l_2)P_4)\lambda_c^2)\sin(a\lambda_c)}{4EJ_1D_1} \end{aligned} \tag{5.56}$$

$$\begin{aligned} C_{10} = {} & \frac{1}{1_2EJ_1D_1}(l1(-4aJ_4l_1(l_1 + 3l_2)P\lambda_c cos(a\lambda_c) + \\ & + (-4l_1(3aJ_1 + J_3(l_1 + 3l_2))P)\sin(a\lambda_c) + \\ & + (6aHJ_1P_4 + aJ_4(2l_1l_2(2l_1 + 3l_2)P + \\ & + H(2l_1^2 + 6l_1l_2 + 3l_2^2)P_4)\lambda_c^2)\sin(a\lambda_c))) \end{aligned} \tag{5.57}$$

$$C_{11} = 0 \tag{5.58}$$

$$C_{12} = C_6 \tag{5.59}$$

$$C_{13} = 0 \tag{5.60}$$

$$C_{14} = \frac{(2l_1P - HP_4)\sin(a\lambda_c)}{4ED_1} \tag{5.61}$$

$$C_{15} = \frac{a(-2l_1P + HP_4)\sin(a\lambda_c)}{2ED_1} \tag{5.62}$$

$$\begin{aligned} C_{16} = {} & \frac{1}{6EJ_1D_1}(-aJ_4l_1(2l_1^2 + 6l_1l_2 + 3l_2^2)P\lambda_c cos(a\lambda_c) + \\ & + -J_3l_1(2l_1^2 + 6l_1l_2 + 3l_2^2)P)\sin(a\lambda_c) + \\ & + (a(l_1 + l_2)(-6J_1l_1P + 3HJ_1P_4 +))\sin(a\lambda_c) \\ & + a(l_1 + l_2)(J_4(l_1l_2(2l_1 + l_2)P + \\ & + H(l_1 + l_2)^2P_4)\lambda_c^2))\sin(a\lambda_c)) \end{aligned} \tag{5.63}$$

$$C_{17} = \frac{P_4}{A_3 E} \tag{5.64}$$

$$C_{18} = \frac{-aP_4}{A_3 E} \tag{5.65}$$

$$\begin{aligned}
C_{19} =& \frac{1}{6EJ_1\lambda_c D_1}(a(J_1(6l_1P - 3HP_4) - \\
&+ J_4 l_1(2l_1^2 + 6l_1l_2 + 3l_2^2)P\lambda_c^2)cos(a\lambda_c) + \\
&+ \lambda_c(-J_3 l_1(2l_1^2 + 6l_1l_2 + 3l_2^2)P)\sin[a\lambda_c] + \\
&+ \lambda_c(a(l_1 + l_2)(-6J_1l_1P + 3HJ_1P_4))\sin[a\lambda_c] \\
&+ \lambda_c(a(l_1 + l_2)(J_4(l_1l_2(2l_1 + l_2)P + \\
&+ H(l_1 + l_2)^2 P_4)\lambda_c^2))\sin[a\lambda_c])
\end{aligned} \tag{5.66}$$

$$C_{20} = 0 \tag{5.67}$$

$$C_{21} = \frac{a(-2l1P + HP4)\sin(a\lambda_c)}{2EJ_1\lambda_c D_1} \tag{5.68}$$

$$C_{22} = \frac{a(-2l1P + HP4)cos(a\lambda_c)}{2EJ_1\lambda_c D_1} \tag{5.69}$$

$$C_{23} = \frac{(aP_4)}{(A_4E)} + \frac{a^3(-2l_1P + HP_4)^2}{16E^2(D_1)^2} \tag{5.70}$$

where

$D_1 = -aJ_4\lambda_c cos(a\lambda_c) + D_2\sin(a\lambda_c)$

$D_2 = -J_3 + aJ_4(l_1 + l_2)\lambda_c^2$

From the boundary condition $w_2(l_2) - \frac{H_2}{2}\phi_2(l_2) = w_4(0)$, we obtain a second degree equation for the auxiliary unknown, P. Just by solving this non linear equation, we obtain two roots of P, but a part of this root must be excluded because, in four-point bending test, P is always downward (positive) and never upward (negative). The previous equation could be written in this form:

$$\alpha P^2 + \beta P + \gamma = 0 \tag{5.71}$$

5.4 Prediction of delamination growth

In the post-critical stage, we expect to witness a progressive increase in the interfacial stresses, eventually leading to further growth of the delamination crack. Both normal and tangential stresses are present at the crack tips, fracture will occur under I/II mixed-mode conditions. To predict the onset of delamination growth, we first evaluate the energy release rate and mode mixity. Then, we compare the available energy release rate with the critical value according to the criterion of Hutchinson and Suo [40]. To evaluate the energy release rate, we adopt the method proposed by Valvo [85] for delaminated beams. Accordingly, the energy release rate for mode I and mode II are a functions of the internal forces at the crack tip $N_1^C, Q_1^C M_1^C, N_2^C, Q_2,^C, M_2^C$.

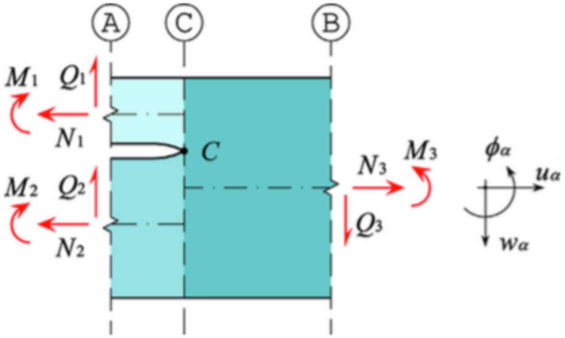

Figure 64: Internal forces and generalized displacement convention [85].

In particular, for a unidirectional laminated beam, the mode I and II contributions are:

$$
\begin{aligned}
G_I =& \frac{3}{8B^2 * E_x} \left(H_1 - H_2\right)^2 \frac{H_1 H_2}{H^3} \left(\frac{N_1^C}{H_1} - \frac{N_2^C}{H_2}\right)^2 + \\
&+ \frac{3}{5B^2 G_z x} \frac{H_1 H_2}{H} \left(\frac{Q_1^C}{H_1} - \frac{Q_2^C}{H_2}\right)^2 + \\
&+ \frac{3}{2B^2 E_x} \frac{H_1 H_2}{H^3} \left(\frac{3H_1 + H_2}{H_1^2} M_1^C - \frac{H_1 + 3H_2}{H_2} M_2^C\right)^2
\end{aligned} \tag{5.72}
$$

$$
G_{II} = \frac{1}{8B^2 * E_x} \frac{H_1 H_2}{H} \left(\frac{N_1^C}{H_1} - \frac{N_2^C}{H_2}\right)^2 + \frac{9}{2B^2 E_x} \frac{H_1 H_2}{H} \left(\frac{M_1^C}{H_1^2} + \frac{M_2^C}{H_2^2}\right)^2 \tag{5.73}
$$

Here, for the four-point bending specimen:

$$N_1^C = N_4(0) \tag{5.74}$$

$$Q_1^C = T_4(0) \tag{5.75}$$

$$M_1^C = M_4(0) \tag{5.76}$$

$$N_2^C = N_3(0) \tag{5.77}$$

$$Q_2^C = T_3(0) \tag{5.78}$$

$$M_2^C = M_3(0) \tag{5.79}$$

where the stresses are valued in $s_3 = s_4 = 0$

The total energy release rate is:

$$G = G_I + G_{II} \tag{5.80}$$

Furthermore, we compute the mode-mixity angle as follows:

$$\phi = \arctan \sqrt{\frac{G_{II}}{G_I}} \tag{5.81}$$

According to Hutchinson and Suo's fracture criterion [40], the critical value of G is estimated by the formula

$$G_C(\phi) = \frac{1}{\frac{\cos^2(\phi)}{G_{IC}} + \frac{sin^2(\phi)}{G_{IIC}}} \tag{5.82}$$

Crack propagation is expected when $G \geq G_C(\phi)$.

5.5 Conclusions

With the previously reported equations, we are able to describe the non linear elastic behavior of the laminated specimen subjected to a four-point bending test, with a central and symmetrical through-the-width delamination. Furthermore, we are able to evaluate the onset of delaminations, by comparing the energy release rate with the Hutchinson and Suo's [40] fracture criterion. In addition, we want to underline that:

- it was experimentally observed, during the linear elastic phase, that there is contact between sub - laminates ④ and ③, but our mechanical model does not take into account this contact. However, the mechanical model allows interpenetration between sub - laminates ④ and ③, but interpenetration is neglected. In the following chapter, contact and interpenetration conditions are given just by eliminating the portions of load path that are physically impossible;
- our mechanical model considers just the onset of delamination for a given crack length $a = cost$, but if we vary the crack length a, we are also able to describe the propagation phase in a quasi-static manner. However, experimental evidence suggests that the propagation is dynamic. This question proposes further investigation.

Chapter 6

Results and discussion

6.1 Comparison with test at MUSAM Lab

In present chapter, we use the previously presented mechanical model to describe the behavior of tested specimens. In particular, we apply the mechanical model to a specimen with the mean values of geometric dimension and mechanical characteristic of tested specimens, that we have presented in Chapter 4. Table 8 summarizes the the geometric dimension of the specimen and Table 9 summarizes the the mechanical characteristics. The elastic modulus and mode I fracture toughness are given by Microtex Composites S.r.l., which is the specimens producer. Mode II fracture toughness is evaluated by the present author with the facilities of MUSAM Lab at IMT Lucca, with the results presented in Chapter 3.
Our mechanical model furnishes acceptable predictions only if there is no contact and interpenetration between the sub-laminates ③ and ④. For this reason, appropriate constraints are introduced in the following chapter. Furthermore, we compare the analytical prediction with experimental evidence.

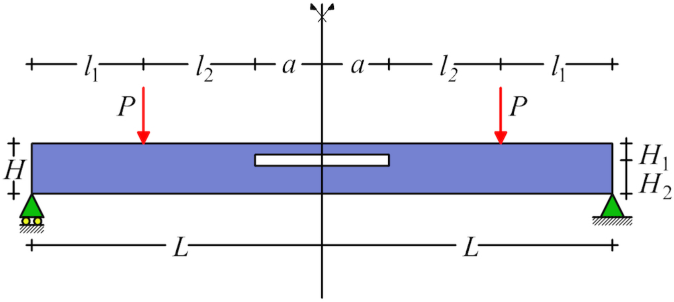

Figure 65: Geometric characteristic of the FPB specimens

Table 8: Geometric properties of the FPB specimens

H (mm)	a (mm)	l_1 (mm)	l_2 (mm)	H_1 (mm)	H_2 (mm)	B (mm)
5.26	20	50	50-a	$H/8$	$H - H_1$	12.89

6.1.1 Geometric and mechanical characteristics of specimens

The mean values of the geometric characteristic of the specimens are summarized in Table 8. The mechanical properties of the specimens are summarized in Table 9, with more details reported in Chapter 3.

Table 9: Mechanical properties of the FPB specimens

E [GPa]	G_{IC} [J/m^2]	G_{IIC} [J/m^2]
129.5	812	1978.5

6.1.2 Analytical predictions

Before solving the equation (5.71), we are going to study the sign of the discriminant $\Delta = \beta^2 - 4\alpha\gamma$. As shown in Figure 67 depending on the values of P_4, the discriminant can be either be positive, negative, or null. Figure 68 shows a magnification of the part of the plot within the box in Figure 67.

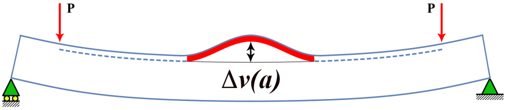

Figure 66: Delaminated specimen

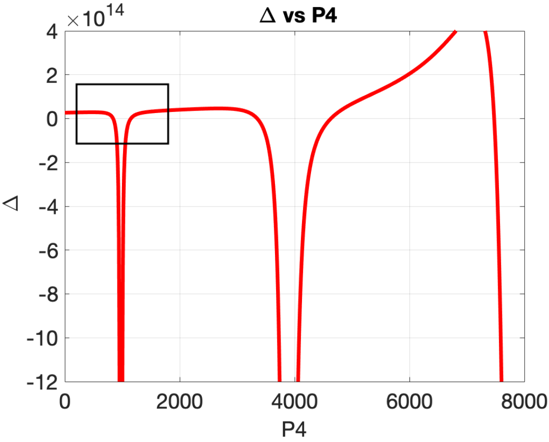

Figure 67: Discriminant Δ vs. axial force, $P4$, of the sub-laminate ④

Correspondingly, the roots of the equation ((5.71)), representing the applied load, can be real or imaginary; for obvious reasons, the imaginary roots must be eliminated. The imaginary part arrives from the particular solution strategy that we have adopted to overcome the non linearity: the applied load became an auxiliary unknown, and the solution was represented as functions of the axial stress, $P4$, the axial load of the sub-laminate ④.

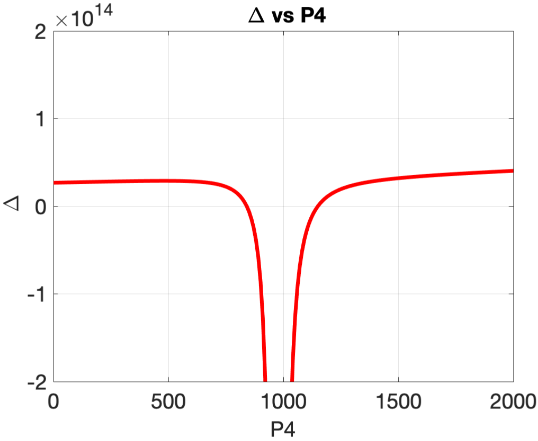

Figure 68: Zoom of the squared portion of discriminant Δ vs. axial force, $P4$, of the sub-laminate ④

In Figure 69, we can distinguish three zones: I, II and III. In zones I and III we have two real and distinct roots for the applied load P; in zone II, the applied load P corresponds to two complex conjugates roots.

To better explain the proposed solution in Figures 70, 71 and 72, we can see respectively: the trend of the applied bending moment as function of the axial force, $P4$, of the sub-laminate ④; the applied load as functions of the axial force, $P4$, of the sub-laminate ④; the relative displacement between the sub-laminates ③ and ④ as function of the axial force, $P4$, of the sub-laminate ④.

If we focus our attention in the squared portion of the graphs reported in Figures 70, 71 and 72, that represent the portion with feasible value for the axial force, $P4$, of the sub-laminate ④, we obtain the graphs reported in Figures 73, 74 and 75. Obviously, there is a first zone I, further subdivided into $I - a$ e $I - b$, where the root of the applied load are real and distinct, as we can see in Figures 73 and 74. If we focus our attention to Figure 75, we can see at a small value of of $P4$, there is interpenetration

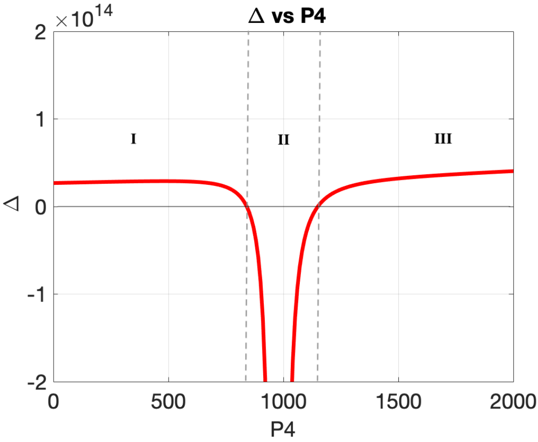

Figure 69: Closer examination of discriminant Δ vs. axial force, $P4$, of the sub-laminate ④

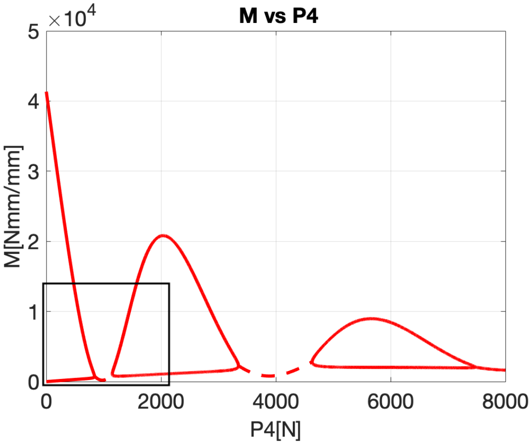

Figure 70: Applied bending moment vs. axial force, $P4$, of the sub-laminate ④

between sub-laminates ③ and ④, both for the path $I - a$ and $I - b$. The first path (I) must be excluded from the solution because the interpenetration is unfeasible. The second path (II) is unfeasible because the roots

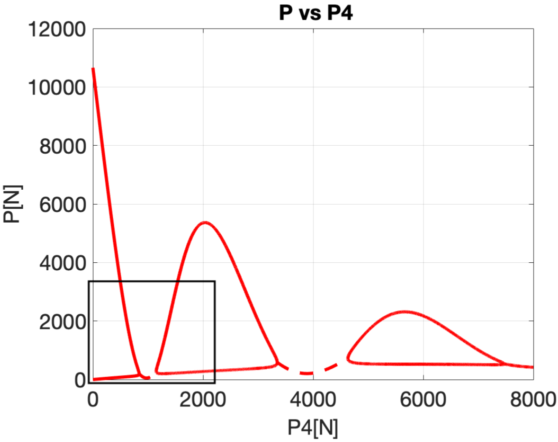

Figure 71: Applied force vs. axial force, $P4$, of the sub-laminate ④

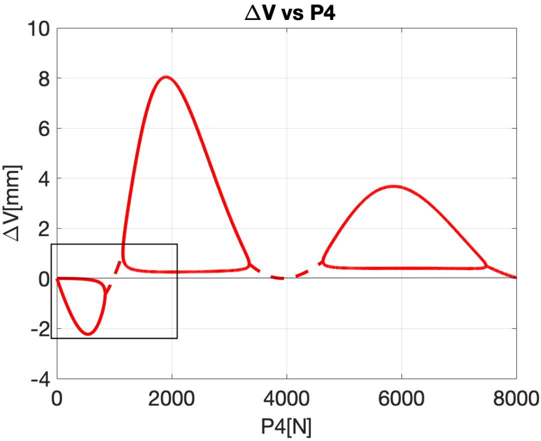

Figure 72: Relative displacement between the sub-laminates ③ and ④ vs. axial force, $P4$, of the sub-laminate ④

of the applied load P is complex conjugate, and in Figures 73, 74 and 75, we can see just the real part of the roots, represented with dashed lines that coincide.

In Figure 76 is reported the bending moment, $M = Pl_1/b$, vs. the

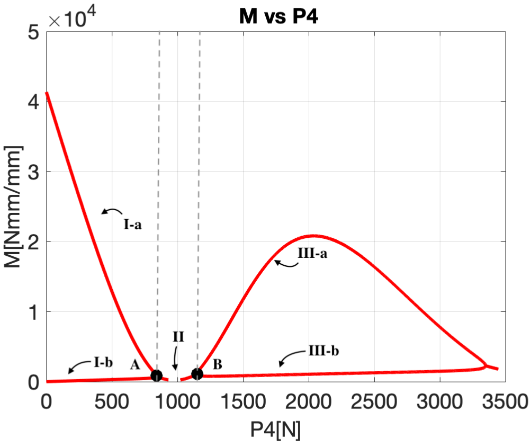

Figure 73: Applied bending moment vs. axial force, $P4$, of the sub-laminate ④

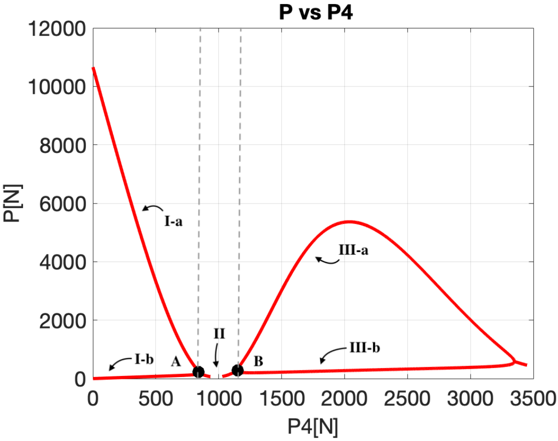

Figure 74: Applied force vs. axial force, $P4$, of the sub-laminate ④

relative displacement between the sub-laminates ③and ④, (a), at the mid-span cross section. The curves shown in Figure 76 represent all theoretical solution points. However, at a closer examination, it appears that some portions of the solution curves must be excluded because they rep-

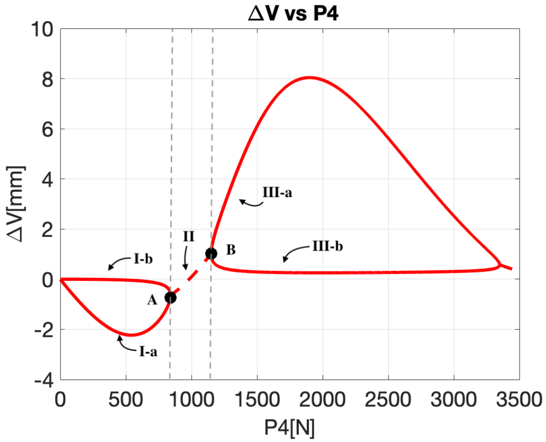

Figure 75: Relative displacement between the sub-laminates ③ and ④ vs. axial force, $P4$, of the sub-laminate ④

resent physically unfeasible states. As previously described, the paths $I-a$ and $I-b$ are characterized by $\Delta V \leq 0$, so these solutions are unfeasible. Path II is characterized by complex conjugate values for the applied load and must be eliminated.

Finally, we arrive at the desired physically feasible solution paths: $III-a$ and $III-b$. Figure 77 corresponds to Figure 76 without the unfeasible paths. The unfeasible paths are represented by yellow lines, and the feasible ones by a continuous red line. In the pre-critical path we assume, as it was experimentally observed, that sub-laminates ③ and ④ stay in contact until buckling occurs (it was also experimentally observed by many researchers [38, 39, 48, 49, 50, 44]). Also in line with experimental evidence, we expect that instability will not occur through equilibrium bifurcation, but by snapping.

In Figure 78, which reports the axial force, $P4$, of the sub-laminate ④ vs. $\delta = v_2(0)$, there is a linear-elastic portion from the origin until the C point, where the pre-buckling path meets the post-buckling path $III-b$. As described in Chapter 5, the specimen in the pre-buckling path has the same behavior of an intact specimen. In fact, between the load application point, the shear force is zero. When $P4$ reaches the C point ($P4 = 1814$N), the sub-laminate ④ buckles and the specimen loses stiffness until C' point ($P4 = 1151$N). Increasing the load, we can observe an increasing of displacement of the load application point, δ, without an increase of the axial force of the sub-laminate ④.

Finally, in Figure 79, the feasible path, III, is represented with the pre-buckling path, $0 - C - C'$, of the applied bending moment, $M = Pl_1/b$, vs. the relative displacement between the sub-laminates ③and ④, (a), at the mid-span cross section. We can see that in the pre-buckling path, sub-laminates ③ and ④ stay in contact ($\Delta V = 0$) until buckling occurs and the sub-laminates ④ snaps upwards from the C point ($M = 984$ Nmm/mm) to until the C' point($M = 986$ Nmm/mm). In Figure 80, to validate our mechanical model, we have plotted with blue dotted lines the experimental results conducted by the present author at MUSAM Lab and presented in Chapter 4.

We can observe, in experimental data, that in the pre-buckling path it is not completely equal to zero due to nail imperfection (0.63mm). In fact, the experimental data are moved to the right by the thickness of the imperfection (0.63mm). In the post-buckling configuration, the experimental data tend to analytical solution, but the buckling load occurs before the analytical prediction due to the imperfection.

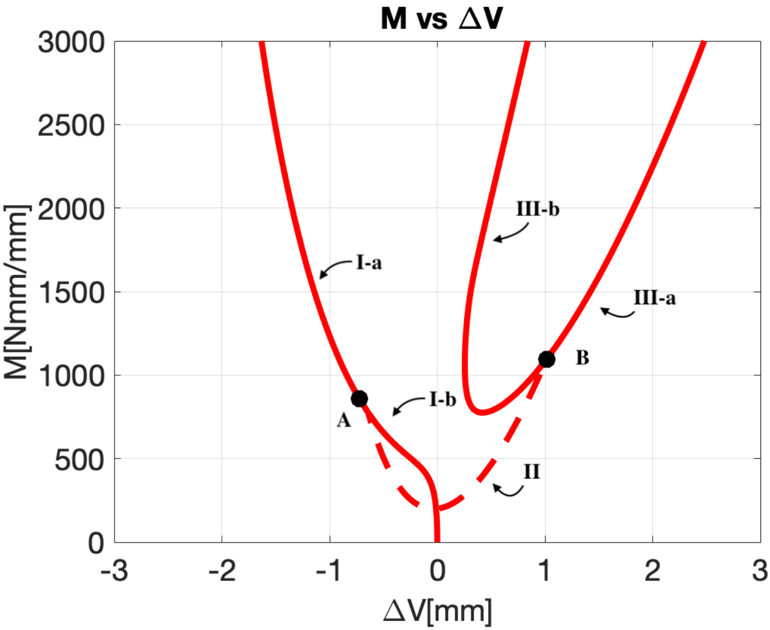

Figure 76: All paths of the applied bending moment vs. relative displacement between the sub-laminates ③ and ④.

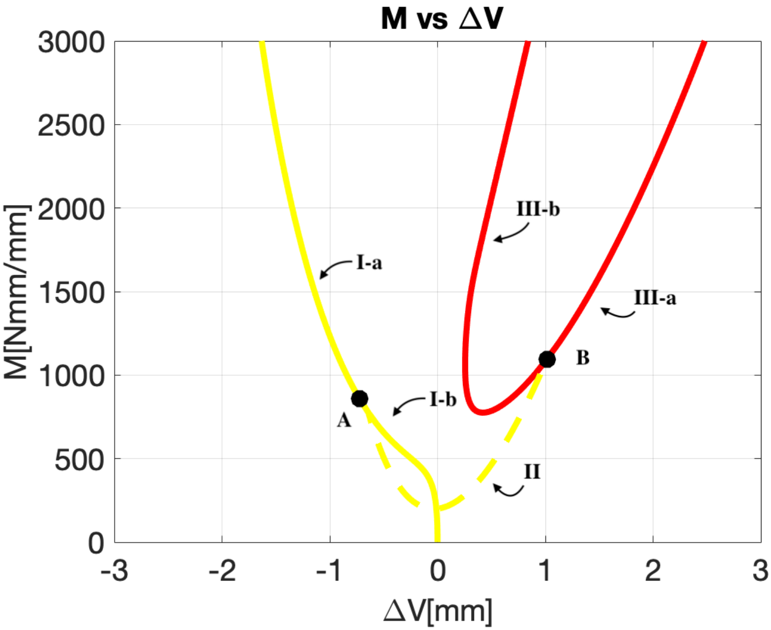

Figure 77: Applied bending moment vs. relative displacement between the sub-laminates ③ and ④.

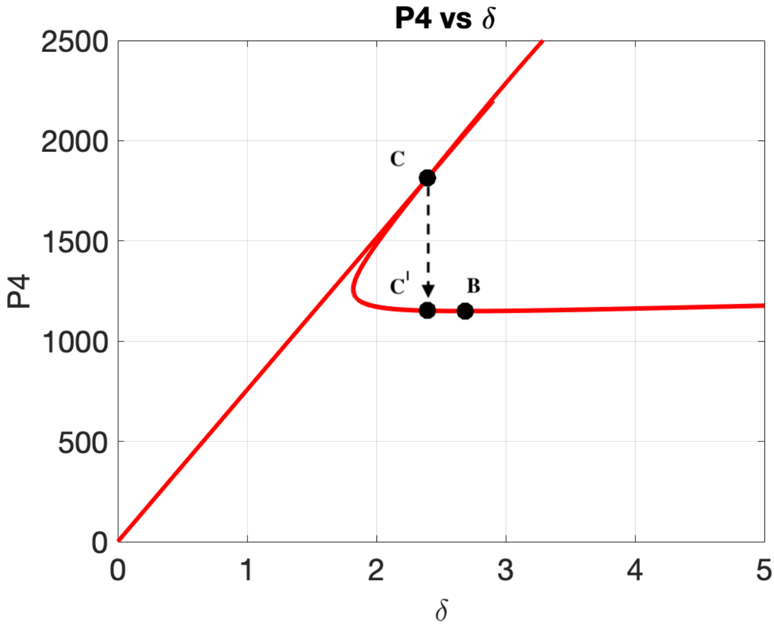

Figure 78: Axial force, $P4$, of the sub-laminate ④ vs. $\delta = v_2(0)$

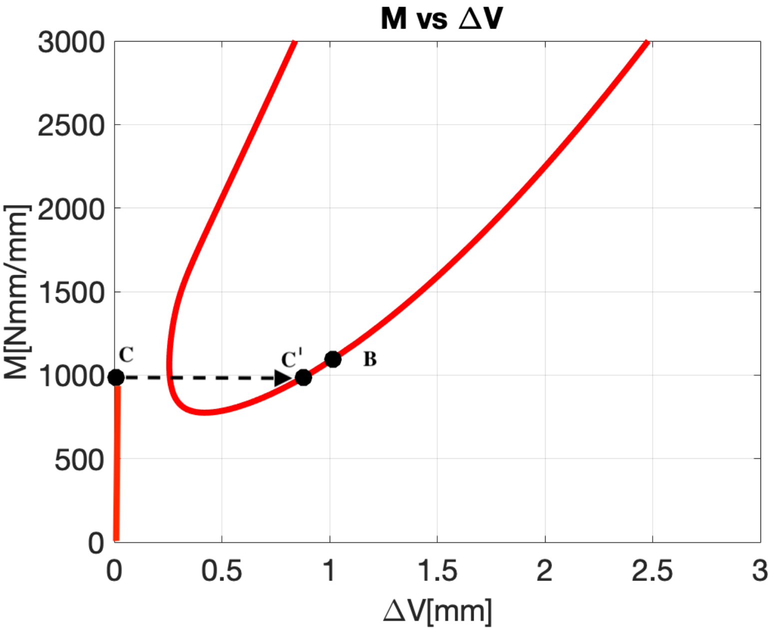

Figure 79: Applied bending moment vs. relative displacement between the sub-laminates ③ and ④.

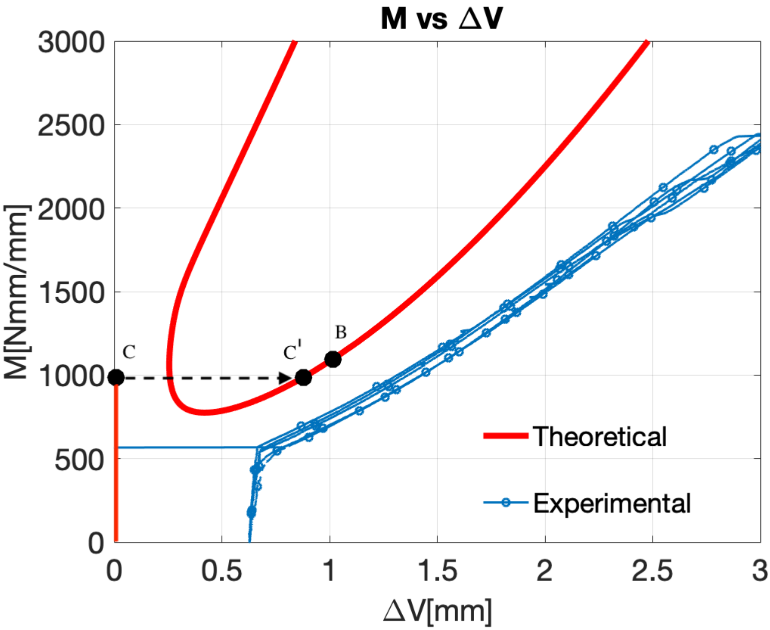

Figure 80: Comparison between th experimental results and the proposed mechanical model

6.1.3 Prediction of delamination growth

In the post-critical stage, we expect a progressive increase in the interfacial stresses, eventually leading to further growth of the delamination crack. Since both normal and tangential stresses are present at the crack tips, fracture will occur under I/II mixed-mode conditions. To predict the onset of delamination growth, we first evaluate the energy release rate and mode mixity. In Figure 81, a photo of the crack tip can be observed, made with 3D confocal-interferometric profilometer (LEICA, DCM 3D) used as a 10x strength microscope.

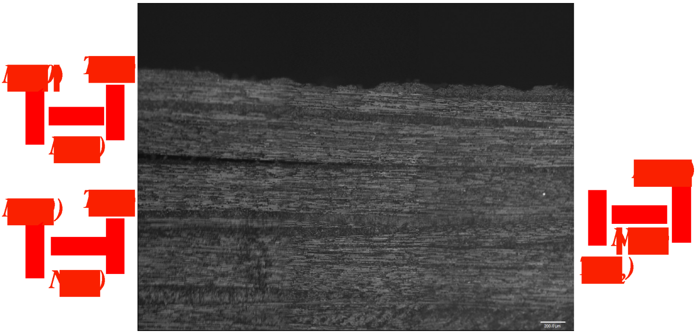

Figure 81: Internal forces at the crack tip

Figure 82 shows a plot of the available (red curve) and critical (green curve) energy release rates as functions of the compressive axial force in sub-laminate ④. The intersection point D between the two curves (after excluding the unfeasible path), corresponds to the predicted onset of delamination growth. In this numerical example, delamination growth for the value of $P4$, is expected to be about 1200N, corresponding to an applied bending moment M = 2460 Nmm/mm. This value is very close to the bending propagation moment that was measured experimentally as can be observed in Figure 83.

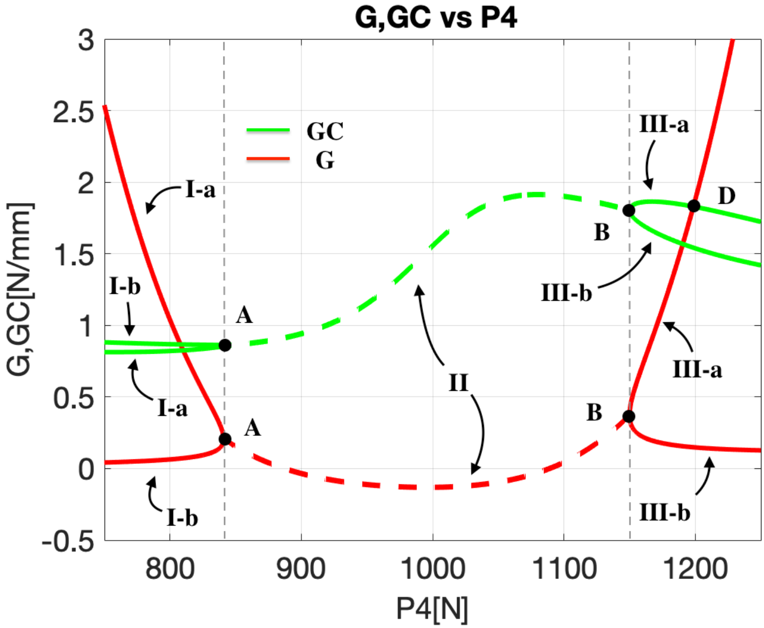

Figure 82: Energy release rate versus fracture toughness

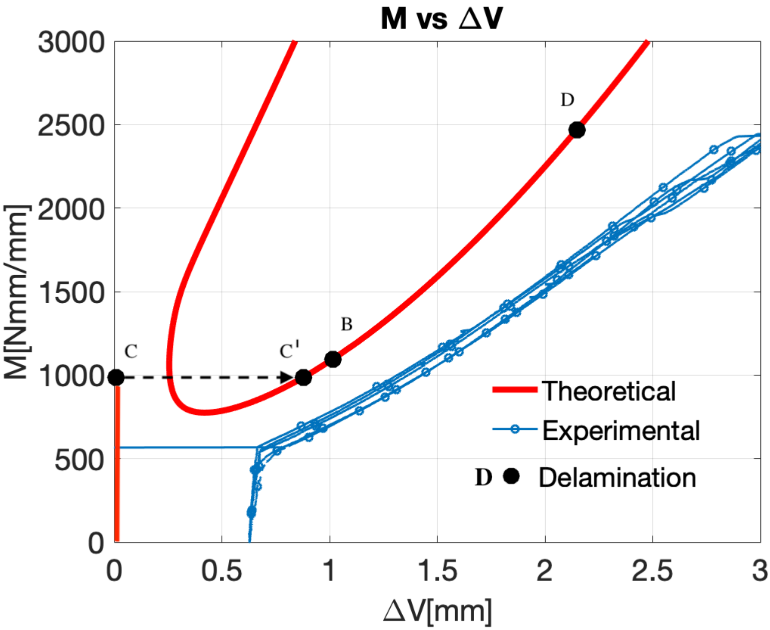

Figure 83: Comparison between experimental results and the proposed mechanical model

6.2 Comparison with the model by Kinawy *et al.*

Here, a comparison between the proposed mechanical model, presented in Chapter 5, and the model proposed by Kinawy *et al.* is reported. The comparison is possible due to the availability of Kinawy's specimens data [48]. In particular, the mechanical model is applied to a delaminated beam manufactured from 16 layers of unidirectional $M21 - T800$ FRP. The specimen, as reported in [48], was assumed to have an average thickness of 4.22 mm and a central through-with-delamination of 40 mm length situated between the second and the third layer. The average layer thickness and the Young's modulus used were 0.26 mm and 155 GPa. As it is possible to see in Figure 84 there is a good agreement between the model proposed in the present thesis and Kinawy's model. In particular, it is noted that the proposed model shows a shows a lower stiffness for $\Delta V > 0$. This discrepancy could arise from the fact that the Kinawy's model it is focused only on the delaminated portion of the beam and due to the fact that the Kinawy's model a priori assumes the shape of the buckled configuration.

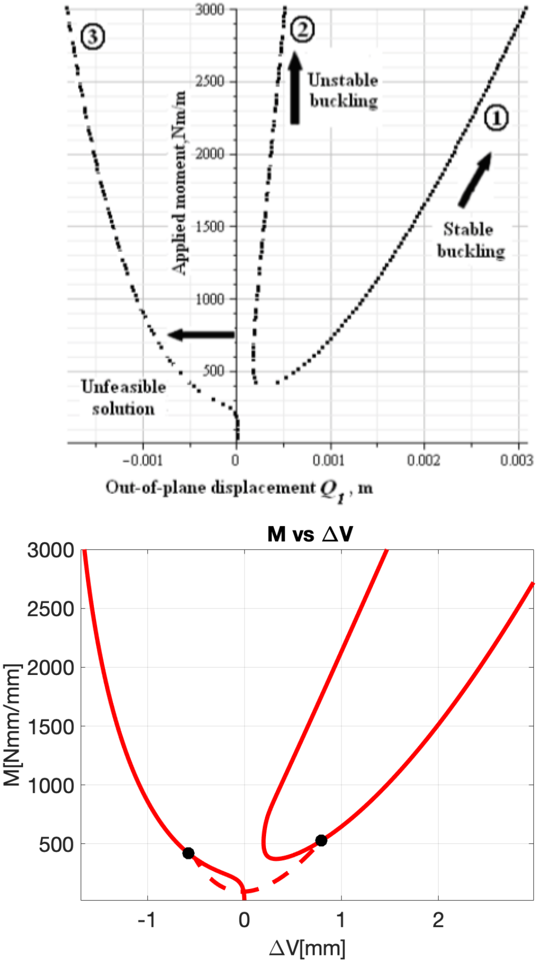

Figure 84: Comparison with Kinawy's model [48]

Chapter 7

Conclusions and future developments

7.1 Summary and conclusions

Summarizing, thanks to the developed model it is possible to describe the non linear elastic behavior of the laminated specimen subjected to a four-point bending test, with a central, symmetrical through-the-width delamination. Furthermore, thanks to a mixed mode fracture analysis, it is possible to evaluate the onset of delaminations, by comparing the available energy release rate with the critical energy release rate, as given for instance by Hutchinson and Suo [40] mixed mode fracture criterion.
The presented approach introduces an innovation to find a solution of this kind of non linear problems. In fact, the adopted solution strategy overcomes the non linearity of the last boundary condition, by considering the applied load (P) as an unknown. Then, the solution is rebuilt as a function of the axial force ($P_4 = -C_{24}$) of the sub-laminate ④.
Another innovative aspect, presented in Chapter 4, was the applications of the backward Digital Image Correlation to measure the displacement field. As previously described, the area of the interest, in which to focus the image processing, was set starting from the final deformed configuration of the four-point bending test. This procedure solves the problems

caused by the upward snapping of the sub-laminate ④, where a classical frontward DIC loses the area of interest focused on the sub-laminates ④. Thanks to this procedure, it is possible to measure the relative displacement between the upper and the lower sub-laminates.

7.2 Future developments

Starting from the work developed in the present thesis several research trails are opened, for instance:

- it was experimentally observed, during the linear elastic phase, that there is contact between sub-laminates ④ and ③, but our mechanical model doesn't take into account directly this contact. As future development, it could be possible to develop a model that takes into account directly the contact phase, is it also using a FEM approach;
- our mechanical model was developed just until the onset of delamination for a given crack length $a = cost$, but if we vary the crack length a, we are also able to describe the propagation phase in a quasi-static manner, but experimental evidence suggests that the propagation is dynamic;
- observing all available four-point tests presented in literature and conducted at MUSAM lab, it is worth noticed that also the stability of the propagation could play an important role. Also this question proposes further investigation.

Appendix A

The effect of spatially nonhomogeneous bonding properties

A.1 Introduction to peeling test

The previous chapters have highlighted the fundamental interplay between fracture mechanics and geometrical instability caused by compressive stress states. In that regard, the joint adhesive energy and its strength do play a fundamental role. So far, for modelling reasons, the fracture mechanics parameters of the interfaces have been assumed to be the same everywhere. However, local imperfections and spatial variabilities of adhesive properties may perturb the overall response.

Here, we study the problem of interface properties variabilities in relation to a real case study of industrial interest, which relates to the soldering of busbars used in photovoltaics. The quality of soldering between silver-coated copper busbars on silicon solar cells is important to assure a proper electric behavior of a photovoltaic module. However, due to the microscopical texture of the surface of the solar cells and imperfect thickness of the soldering paste, the adhesion between the busbar and silicon is never uniform and perfect. The results of peeling tests reported in the literature [53] and also independently carried out by the present authors using the facilities of the Multi-scale Analysis of Materials laboratory (MUSAM-Lab) of IMT, have shown that the peeling force vs. displacement curve is not smooth and presents several jumps, as we can see in Figure 85.

In this study, to characterize soldering for this specific technological problem and to also develop a new theoretical framework for modeling and simulation of the nonlinear fracture response of interfaces with imperfect bonding or adhesion, a fracture mechanics model based on the theory of a beam on an elastic foundation is proposed. In this framework, the busbar is modeled as an Euler-Bernoulli beam connected to the rigid substrate by an elastic interface which may undergo brittle failure, in line with the method formulated in [65, 23] for the double cantilever beam test.

To take into account a variability of bonding parameters in the mathematical formulation, an effective fracture toughness dependent on the position along the interface is introduced. In order to identify such a function, a careful analysis of the delaminated interface of a busbar from silicon obtained from a peeling test, has been performed using the LEICA DCM3D confocal profilometer. This analysis reveals that the delamination crack propagates in a zig-zag manner, from the interface between the silicon and the soldering paste, to the interface between the soldering paste and the busbar. Across the width of the busbar, both paths are also possible.

Setting two different values for the fracture toughness corresponding to such types of delamination (between the silicon and the soldering paste, or between the soldering paste and the busbar), the effective fracture toughness in a point along the interface is assumed to be a linear function of those, weighted by the corresponding relative amount of crack path observed through the busbar width. The proposed model, tuned based on the experimental peeling test results, can be profitably used to establish lower and upper bounds to the effective toughness of the silicon-busbar interface; accurately reproducing the force-displacement curve of the peeling tests with imperfect interfaces.

A.2 Peeling test

The peeling test was conducted by pulling out the busbar at an angle of 90 degrees at the speed of 0.1mm/sec. Here, we propose a new framework to characterize the soldering quality: starting from an image analysis based criterion for the assessment of the interface fracture energy, we pass on a confocal profilometer analysis to analyse the fracture pattern and its roughness.

Figure 85: Busbar peeling test conducted at Musam Lab of IMT

A.3 Interface characterization: image analysis based criterion

In Figure 2 we can see the solar cell, the delaminated portion on the solar cell and the peeled busbar. We focus our attention on the interface from the solar cell side, because it is smoother than the peeled busbur as we can see in Figure 86. Furthermore, we converted the photo of the interface to a black and white one (Figure 87).

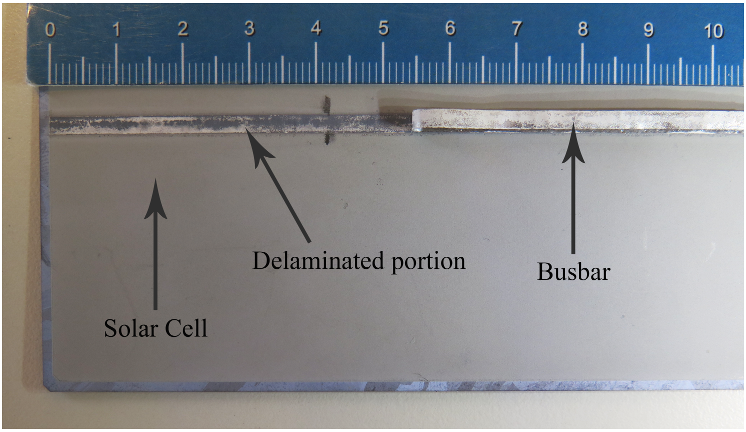

Figure 86: Photo of the delaminated interface on the solar cell

Thus, we pass to the confocal profilometer (LEICA DCM3D) analysis in order to thoroughlyl understand the crack pattern and its roughness (Figure 88,89). From the photo, we observe that the white portion is the soldering paste that remains attached to the solar cell; the black portion represents the silicon solar cell. From here, we process process the Figure 88 from a quantitative point of view by conducting an image analysis.

The black and white image, observed in Figure 87, has been transformed in a matrix of 0 and 1, where zeros represent the silicon (black pixel) and ones represent soldering paste (white pixel). In the graph in Figure 90, we report the sum of the elements of each colon of the black and white matrix. Thanks to this, we know which is 55 mm long. In addition to this, we assume that the soldering paste distributions on the peeled busbar is complementary to this distribution.

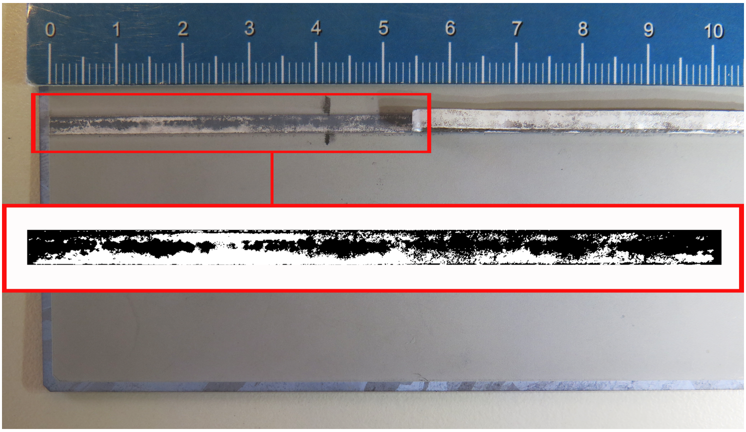

Figure 87: Photo of the delaminated interface on the solar cell and black and white conversion

A.4 Mechanical model

Let us consider a busbar of length l, and thickness h, connected with a rigid substrate by an elastic interface [84, 87, 67]. The busbar is peeled from a rigid substrate by using an increasing force P, which is applied to the left free edge. The busbar is modeled as a flexible and inextensible Eulero-Bernoulli beam. Instead, the solar cell is a rigid substrate due to the fact that the peeling machine neglect the deformation.

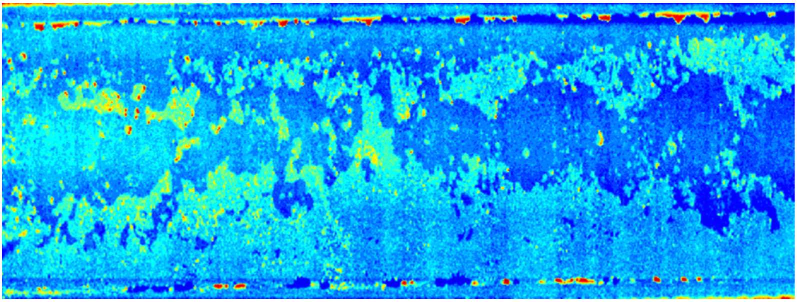

Figure 88: Confocal profilometer plane view

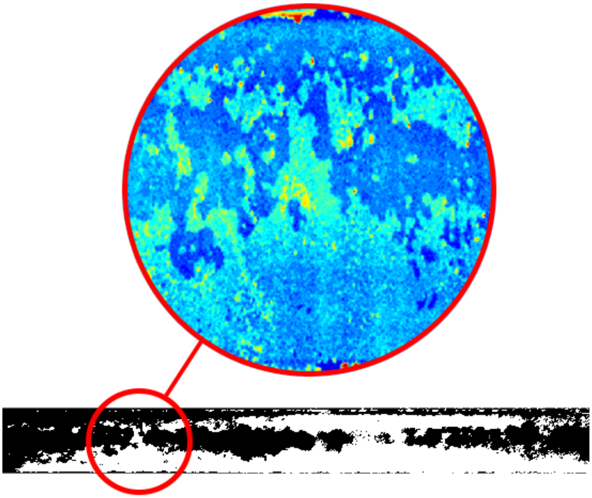

Figure 89: Zoom on the interface photo

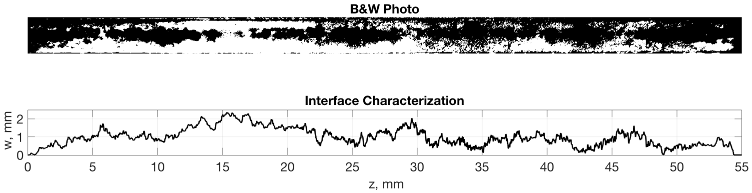

Figure 90: Interface characterization

Let $v(z)$ and $\phi(z)$, respectively denote the transverse displacement and

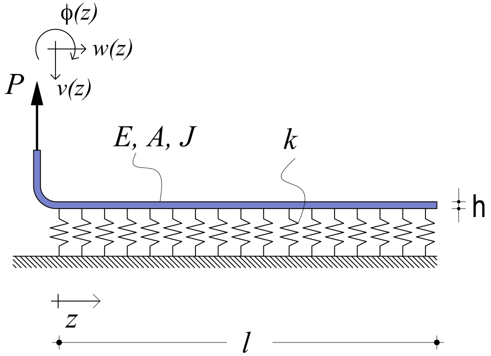

Figure 91: Mechanical model

the rotation (positive if clockwise) of a generic cross-section.
By imposing the equilibrium of an infinitesimal portion of beam as shown in Figure 92.

we obtain the following eqautions:

$$\frac{\mathrm{d}T(z)}{\mathrm{d}z} = p(z) \tag{A.1}$$

$$\frac{\mathrm{d}M(z)}{\mathrm{d}z} = T(z) \tag{A.2}$$

Assuming the following constitutive law for the interface:

$$p(z) = kv(z) \tag{A.3}$$

From the constitutive law:

$$M(z) = -EJv(z)^{II} \tag{A.4}$$

After differentiating eq. A.2, and substituting the constitutive law, we obtain the following fourth order ordinary differential equation:

$$EJv(z)^{IV} + kv(z) = 0 \tag{A.5}$$

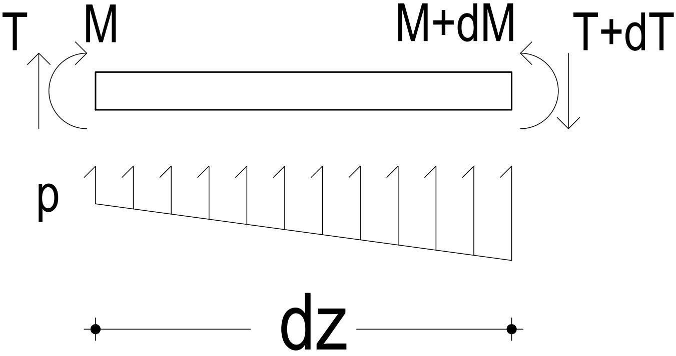

Figure 92: Infinitesimal portion of beam

The differential equation needs to be equipped with the following boundary conditions, which guarantee balance and kinematical compatibility at the end cross-sections of the busbar:

$$M(0) = 0 \tag{A.6}$$

$$T(0) = P \tag{A.7}$$

$$M(l) = 0 \tag{A.8}$$

$$T(l) = 0 \tag{A.9}$$

We use such a model to describe the linear elastic phase. The following table identifies the geometric and mechanic characteristics of the busbar. From here, we need to identify the stiffness of the interface.

Table 10: Geometric and mechanic parameter of busbar

h (mm)	l (mm)	B (mm)	E (N/mm^2)	k (N/mm^3)
0.2	100	2.5	51100	to be identified

From the linear elastic phase, by tuning the parameter k, with our experimental results, we can characterize the Young's modulus of the soldering paste. In fact, if we look at the confocal profiometer analysis (Figure 93), we can measure the height of the soldering paste, so the interface Youngs modulus $E = kt$.

A.5 Propagation phase

After the onset of delamination, we neglect the bending stiffness of the beam and if we look at the $P - \delta$ curve, we can estimate the maximum and minimum fracture toughness just by dividing P values by the width of the busbar. These two values correspond, respectively, to the fracture toughness between the soldering paste and the busbar, and the fracture

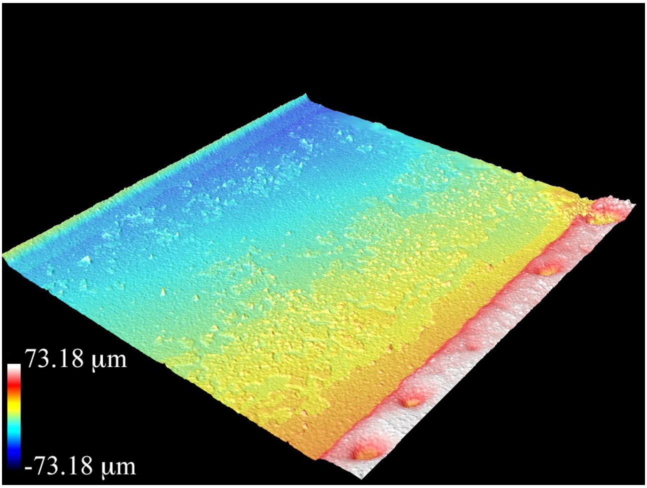

Figure 93: Confocal profilometer 3D view

toughness between the paste and the silicon substrate.

We assume that the distribution of the fracture toughness along the interface is a function of the soldering paste width. For this we associate the value of $G_{\max}$ at $w(z)$, which is the white portions in Figure 90, and $G_{\min}$ to the black portions (which is complementary to the total width). In this scheme, we neglect the contribution of crack growth through the soldering paste in the delamination migration, see Figure 96.

To sum up, in Figure 97 we report the comparison between the peeling test and our model, based on an image analysis criterion. As can be observed, there is a good agreement between the experimental results and the proposed model.

A.6 Conclusions and future developments

An experimental method to assess the fracture energy from image analysis on peeled samples has been developed. This could be used as a post-mortem identification for the quality of soldering of the busbar, for

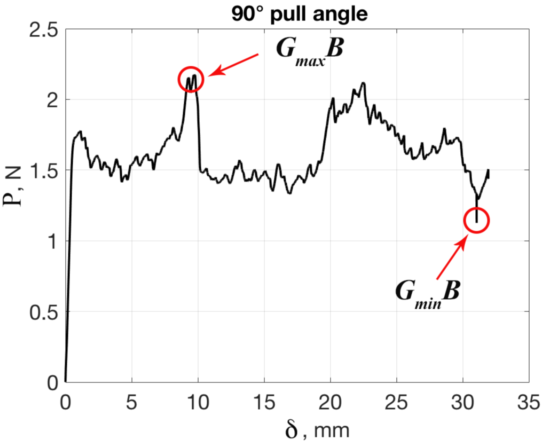

Figure 94: Maximum and minimum fracture toughness values

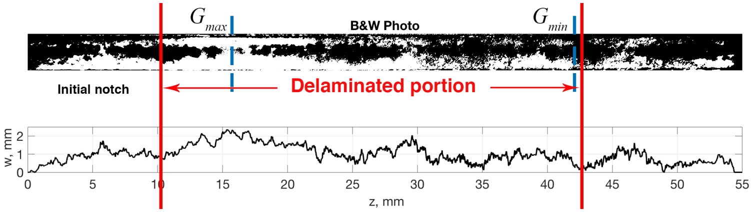

Figure 95: Identifications of the maximum and minimum fracture toughness positions along the interface

instance as a quality test. From profilometer data t, and the identified parameter k, it is possible to assess the Young's modulus of the soldering paste. The experimental trend has been captured by the model as reported in Figure 97. Future developments will include an improved model in order to explicitly take into account possible failures in the soldering paste.

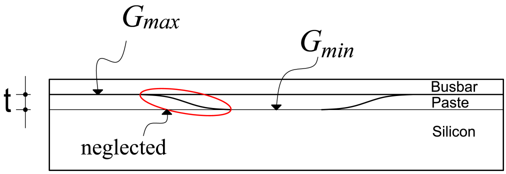

Figure 96: Schematic representation of the fracture toughness distribution through the thickness

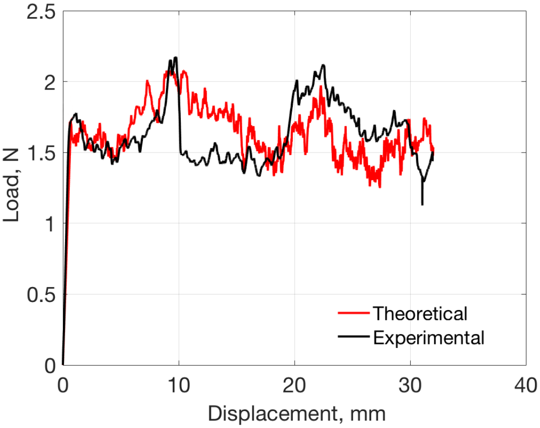

Figure 97: Comparison between our model and the experimental results

Appendix B

Bibliography

[1] Z. Ali, A. A. Kadhim, R. H. Al-Khayat, and M. Al-Waily. Review influence of loads upon delamination buckling in composite structures. *J. Mech. Eng. Res. Dev*, 44:392–406, 2021.

[2] O. Allix and P. Ladevèze. Interlaminar interface modelling for the prediction of delamination. *Composite structures*, 22(4):235–242, 1992.

[3] O. Allix, P. Ladeveze, and A. Corigliano. Damage analysis of interlaminar fracture specimens. *Composite structures*, 31(1):61–74, 1995.

[4] L. B. Andraju, M. Ramji, and G. Raju. Snap-buckling and failure studies on cfrp laminate with an embedded circular delamination under flexural loading. *Composites Part B: Engineering*, 214:108739, 2021.

[5] Y. Arman, M. Zor, and S. Aksoy. Determination of critical delamination diameter of laminated composite plates under buckling loads. *Composites Science and Technology*, 66(15):2945–2953, 2006.

[6] G. Bao and Z. Suo. Remarks on crack-bridging concepts. 1992.

[7] G. I. Barenblatt. The mathematical theory of equilibrium cracks in brittle fracture. *Advances in applied mechanics*, 7:55–129, 1962.

[8] S. Bennati and P. S. Valvo. An elastic-interface model for delamination buckling in laminated plates. In *Key Engineering Materials*, volume 221, pages 293–306. Trans Tech Publ, 2002.

[9] S. Bennati and P. S. Valvo. Delamination growth in composite plates under compressive fatigue loads. *Composites science and technology*, 66(2):248–254, 2006.

[10] S. Bennati, M. Colleluori, D. Corigliano, and P. S. Valvo. An enhanced beam-theory model of the asymmetric double cantilever beam (adcb) test for composite laminates. *Composites Science and Technology*, 69(11-12):1735–1745, 2009.

[11] S. Bennati, P. Fisicaro, and P. S. Valvo. An enhanced beam-theory model of the mixed-mode bending (mmb) testpart i: Literature review and mechanical model. *Meccanica*, 48(2):443–462, 2013.

[12] S. Bennati, N. Dardano, and P. S. Valvo. An elastic-interface model for buckling-driven delamination growth in four-point bending tests. In *AIMETA 2017–23rd Conference of the Italian Association of Theoretical and Applied Mechanics*, volume 4, pages 2107–2118. GECHI EDIZIONI, 2017.

[13] S. Bennati, P. Fisicaro, L. Taglialegne, and P. S. Valvo. An elastic interface model for the delamination of bending-extension coupled laminates. *Applied Sciences*, 9(17):3560, 2019.

[14] H. Bergmann and R. Prinz. Fatigue life estimation of graphite/epoxy laminates under consideration of delamination growth. *International journal for numerical methods in engineering*, 27 (2):323–341, 1989.

[15] V. V. Bolotin. Delaminations in composite structures: its origin, buckling, growth and stability. *Composites Part B: Engineering*, 27 (2):129–145, 1996.

[16] W. Bottega. On thin film delamination growth in a contracting cylinder. *International journal of solids and structures*, 24(1):13–26, 1988.

[17] W. Bottega and A. Maewal. Delamination buckling and growth in laminates. *Journal of Applied Mechanics, Transactions ASME*, 50(1): 184–189, 1983.

[18] A. Brunner, B. Blackman, and P. Davies. A status report on delamination resistance testing of polymer–matrix composites. *Engineering Fracture Mechanics*, 75(9):2779–2794, 2008.

[19] D. Bruno and F. Greco. Mixed mode delamination in plates: a refined approach. *International Journal of Solids and Structures*, 38(50-51):9149–9177, 2001.

[20] D. Bruno and A. Grimaldi. Delamination failure of layered composite plates loaded in compression. *International Journal of Solids and Structures*, 26(3):313–330, 1990.

[21] P. P. Camanho, C. G. Davila, and M. De Moura. Numerical simulation of mixed-mode progressive delamination in composite materials. *Journal of composite materials*, 37(16):1415–1438, 2003.

[22] L. A. Carlsson, D. F. Adams, and R. B. Pipes. *Experimental characterization of advanced composite materials*. CRC press, 2014.

[23] A. Carpinteri, M. Paggi, and G. Zavarise. The effect of contact on the decohesion of laminated beams with multiple microcracks. *International Journal of Solids and Structures*, 45(1):129–143, 2008.

[24] H. Chai, C. D. Babcock, and W. G. Knauss. One dimensional modelling of failure in laminated plates by delamination buckling. *International Journal of Solids and Structures*, 17(11):1069–1083, 1981.

[25] A. Chattopadhyay and H. Gu. Modeling of delamination buckling in composite cylindrical shells with a new higher-order theory. *Composites science and technology*, 54(2):223–232, 1995.

[26] H.-P. Chen and D. Leib. Dynamic delamination growth in laminated composite structures. *Composites science and technology*, 46(4):325–333, 1993.

[27] A. Corigliano. Formulation, identification and use of interface models in the numerical analysis of composite delamination. *International Journal of Solids and Structures*, 30(20):2779–2811, 1993.

[28] A. D7264/D7264M-15. Standard test method for flexural properties of polymer matrix composite materials, 2015.

[29] A. D7905/D7905M-14. Standard test method for determination of the mode ii interlaminar fracture toughness of unidirectional fiber-reinforced polymer matrix composites, 2014.

[30] C. Dahlen and G. S. Springer. Delamination growth in composites under cyclic loads. *Journal of composite Materials*, 28(8):732–781, 1994.

[31] C. Davila, N. Jaunky, and S. Goswami. Failure criteria for frp laminates in plane stress. In *44th AIAA/ASME/ASCE/AHS/ASC Structures, Structural Dynamics, and Materials Conference*, page 1991, 2003.

[32] R. Dimitri, F. Tornabene, and G. Zavarise. Analytical and numerical modeling of the mixed-mode delamination process for composite moment-loaded double cantilever beams. *Composite Structures*, 187: 535–553, 2018.

[33] K. Dransfield, C. Baillie, and Y.-W. Mai. Improving the delamination resistance of cfrp by stitchinga review. *Composites Science and Technology*, 50(3):305–317, 1994.

[34] D. S. Dugdale. Yielding of steel sheets containing slits. *Journal of the Mechanics and Physics of Solids*, 8(2):100–104, 1960.

[35] K. Friedrich. *Application of fracture mechanics to composite materials*. Elsevier, 2012.

[36] A. Giannakopoulos, K.-F. Nilsson, and G. Tsamasphyros. The contact problem at delamination. 1995.

[37] C. Gim. Plate finite element modeling of laminated plates. *Computers & Structures*, 52(1):157–168, 1994.

[38] W. Gong, J. Chen, and E. A. Patterson. An experimental study of the behaviour of delaminations in composite panels subjected to bending. *Composite Structures*, 123:9–18, 2015.

[39] W. Gong, J. Chen, and E. A. Patterson. Buckling and delamination growth behaviour of delaminated composite panels subject to four-point bending. *Composite Structures*, 138:122–133, 2016.

[40] J. W. Hutchinson and Z. Suo. Mixed mode cracking in layered materials. In *Advances in applied mechanics*, volume 29, pages 63–191. Elsevier, 1991.

[41] R. M. Jones. *Mechanics of composite materials*. CRC press, 1999.

[42] L. Kachanov. Delamination of fiberglass tubes under external pressure. *Mekh. Polimerov*, 6:1106–1108, 1975.

[43] M. Kanninen. An augmented double cantilever beam model for studying crack propagation and arrest. *International Journal of fracture*, 9(1):83–92, 1973.

[44] G. Kardomateas. Snap buckling of delaminated composites under pure bending. *Composites science and technology*, 39(1):63–74, 1990.

[45] G. Kardomateas. Predicting the growth of internal delaminations under monotonic or cyclic compression. In *Key Engineering Materials*, volume 120, pages 441–462. Trans Tech Publ, 1996.

[46] G. Kardomateas and C. Chung. Thin film modeling of delamination buckling in pressure loaded laminated cylindrical shells. *AIAA journal*, 30(8):2119–2123, 1992.

[47] G. Kardomateas, A. Pelegri, and B. Malik. Growth of internal delaminations under cyclic compression in composite plates. *Journal of the Mechanics and Physics of Solids*, 43(6):847–868, 1995.

[48] M. Kinawy, R. Butler, and G. Hunt. Buckling and propagation of a delaminated composite beam in bending. In *51st AIAA/ASME/ASCE/AHS/ASC Structures, Structural Dynamics, and*

Materials Conference 18th AIAA/ASME/AHS Adaptive Structures Conference 12th, page 2771, 2010.

[49] M. Kinawy, R. Butler, and G. Hunt. Buckling and postbuckling of a delaminated composite beam in bending. *AIAA journal*, 49(3):670–672, 2011.

[50] M. Kinawy, R. Butler, and G. W. Hunt. Bending strength of delaminated aerospace composites. *Philosophical Transactions of the Royal Society A: Mathematical, Physical and Engineering Sciences*, 370(1965): 1780–1797, 2012.

[51] A. Köllner. Predicting buckling-driven delamination propagation in composite laminates: An analytical modelling approach. *Composite Structures*, 266:113776, 2021.

[52] R. Krueger, K. N. Shivakumar, and I. S. Raju. Fracture mechanics analyses for interface crack problems-a review. In *54th AIAA/ASME/ASCE/AHS/ASC structures, structural dynamics, and materials conference*, page 1476, 2013.

[53] L. Liang, Z. Li, N. Glassmaker, and L. Cheng. Understanding peel force variation during ag bus bar adhesion measurements. In *2014 IEEE 40th Photovoltaic Specialist Conference (PVSC)*, pages 2828–2831. IEEE, 2014.

[54] M. S. Loukil. Microcracking in fiber composites and degradation of thermo-elastic properties of laminates. 2011.

[55] L. Ma, L. Wu, X. Cheng, D. Zhuo, Z. Weng, and R. Wang. Improving the interlaminar properties of polymer composites using a situ accumulation method to construct the multi-scale reinforcement of carbon nanofibers/carbon fibers. *Composites Part A: Applied Science and Manufacturing*, 72:65–74, 2015.

[56] M.-W. Moon. Buckling delamination of compressed thin films. In *Mechanical Self-Assembly*, pages 131–152. Springer, 2013.

[57] T. Nakamura, A. Kushner, and C. Lo. Interlaminar dynamic crack propagation. *International journal of solids and structures*, 32(17-18): 2657–2675, 1995.

[58] B. Pan. Digital image correlation for surface deformation measurement: historical developments, recent advances and future goals. *Measurement Science and Technology*, 29(8):082001, 2018.

[59] K. Park and G. H. Paulino. A critical review of traction-separation relationships across fracture surfaces for cohesive zone models of fracture. *Appl. Mech. Rev.*, 64(6):1002, 2015.

[60] M. Pavier and M. Clarke. A specialized composite plate element for problems of delamination buckling and growth. *Composite structures*, 34(1):43–53, 1996.

[61] S. O. Peck and G. S. Springer. The behavior of delaminations in composite platesanalytical and experimental results. *Journal of composite materials*, 25(7):907–929, 1991.

[62] W. Peters and W. Ranson. Digital imaging techniques in experimental stress analysis. *Optical engineering*, 21(3):427–431, 1982.

[63] W. Peters, W. Ranson, M. Sutton, T. Chu, and J. Anderson. Application of digital correlation methods to rigid body mechanics. *Optical Engineering*, 22(6):738–742, 1983.

[64] A. Pickett, M. Fouinneteau, and P. Middendorf. Test and modelling of impact on pre-loaded composite panels. *Applied Composite Materials*, 16(4):225–244, 2009.

[65] N. Point and E. Sacco. Delamination of beams: an application to the dcb specimen. *International Journal of Fracture*, 79(3):225–247, 1996.

[66] P. Qiao and J. Wang. Mechanics and fracture of crack tip deformable bi-material interface. *International Journal of Solids and Structures*, 41 (26):7423–7444, 2004.

[67] J. Reinoso and M. Paggi. A consistent interface element formulation for geometrical and material nonlinearities. *Computational Mechanics*, 54(6):1569–1581, 2014.

[68] A. Riccio, P. Perugini, and F. Scaramuzzino. Modelling compression behaviour of delaminated composite panels. *Computers & Structures*, 78(1-3):73–81, 2000.

[69] P. Rozylo. Experimental-numerical study into the stability and failure of compressed thin-walled composite profiles using progressive failure analysis and cohesive zone model. *Composite Structures*, 257: 113303, 2021.

[70] S. Sallam and G. Simitses. Delamination buckling and growth of flat, cross-ply laminates. *Composite Structures*, 4(4):361–381, 1985.

[71] B. V. Sankar and S. Hu. Dynamic delamination propagation in composite beams. *Journal of composite materials*, 25(11):1414–1426, 1991.

[72] K. Senthil, A. Arockiarajan, R. Palaninathan, B. Santhosh, and K. Usha. Defects in composite structures: Its effects and prediction methods–a comprehensive review. *Composite Structures*, 106: 139–149, 2013.

[73] G. J. Simitses. Buckling of pressure-loaded, delaminated, cylindrical shells and panels. In *Key Engineering Materials*, volume 120, pages 407–426. Trans Tech Publ, 1996.

[74] G. J. Simitses and Z. Chen. Buckling of delaminated, long, cylindrical panels under pressure. *Computers & structures*, 28(2):173–184, 1988.

[75] B. F. Sørensen and P. Kirkegaard. Determination of mixed mode cohesive laws. *Engineering fracture mechanics*, 73(17):2642–2661, 2006.

[76] B. Storåkers. Nonlinear aspects of delamination in structural members. In *17th Int. Congress of Theoretical and Applied Mechanics*, pages 315–336, 1989.

[77] M. A. Sutton, W. Wolters, W. Peters, W. Ranson, and S. McNeill. Determination of displacements using an improved digital correlation method. *Image and vision computing*, 1(3):133–139, 1983.

[78] M. A. Sutton, J. J. Orteu, and H. Schreier. *Image correlation for shape, motion and deformation measurements: basic concepts, theory and applications*. Springer Science & Business Media, 2009.

[79] A. Szekrenyes. Improved analysis of unidirectional composite delamination specimens. *Mechanics of Materials*, 39(10):953–974, 2007.

[80] A. Tabiei and W. Zhang. Composite laminate delamination simulation and experiment: A review of recent development. *Applied Mechanics Reviews*, 70(3), 2018.

[81] R. Talreja and C. V. Singh. *Damage and failure of composite materials*. Cambridge University Press, 2012.

[82] T. Tay. Characterization and analysis of delamination fracture in composites: an overview of developments from 1990 to 2001. *Appl. Mech. Rev.*, 56(1):1–32, 2003.

[83] J. Thompson and G. Hunt. A general theory of elastic stability. *The Aeronautical Journal*, 79(774):274–274, 1975.

[84] M. Thouless and H. Jensen. Elastic fracture mechanics of the peel-test geometry. *The Journal of Adhesion*, 38(3-4):185–197, 1992.

[85] P. S. Valvo. On the calculation of energy release rate and mode mixity in delaminated laminated beams. *Engineering Fracture Mechanics*, 165:114–139, 2016.

[86] J. D. Whitcomb. Finite element analysis of instability related delamination growth. *Journal of Composite materials*, 15(5):403–426, 1981.

[87] J. Williams and H. Hadavinia. Analytical solutions for cohesive zone models. *Journal of the Mechanics and Physics of Solids*, 50(4):809–825, 2002.

[88] X.-F. Wu and A. L. Yarin. Recent progress in interfacial toughening and damage self-healing of polymer composites based on electrospun and solution-blown nanofibers: An overview. *Journal of applied polymer science*, 130(4):2225–2237, 2013.

[89] Q. Yang and B. Cox. Cohesive models for damage evolution in laminated composites. *International Journal of Fracture*, 133(2):107–137, 2005.

[90] C. W. Yap and G. B. Chai. Analytical and numerical studies on the buckling of delaminated composite beams. *Composite structures*, 80 (2):307–319, 2007.

[91] W.-L. Yin. Energy balance and the speed of crack growth in a compressed plate with delamination. *International journal of solids and structures*, 30(15):2041–2055, 1993.

[92] W.-L. Yin. Thermomechanical buckling of delaminated composite laminates. *International journal of solids and structures*, 35(20):2639–2653, 1998.

[93] X. Zhao. Multifunctional crumpling and unfolding of large-area graphene. *Bulletin of the American Physical Society*, 58, 2013.